Adiabatic theory of strong-field ionization of molecules including nuclear motion: Rescattering

Jens Svensmark,[1] Oleg I. Tolstikhin,[2] and Toru Morishita[1]

[1]*Institute for Advanced Science, The University of Electro-Communications, 1-5-1 Chofu-ga-oka, Chofu-shi, Tokyo 182-8585, Japan*

[2]*Moscow Institute of Physics and Technology, Dolgoprudny 141700, Russia*

(Received 6 October 2021; accepted 3 December 2021; published 16 December 2021)

We extend the adiabatic theory of strong-field ionization of molecules including nuclear motion developed in our previous paper [J. Svensmark *et al.*, Phys. Rev. A **101**, 053422 (2020)] to describe rescattering processes. The adiabatic regime in which the electronic timescale is much smaller than that of the nuclei and laser field is considered. The asymptotics of rescattering parts of the solution to the time-dependent Schrödinger equation (TDSE) and ionization amplitude are obtained, and thus vibrationally resolved photoelectron momentum distributions (PEMDs) in the whole range of the photoelectron momentum are found. The ionization dynamics is described in terms of a nuclear wave packet in the molecular ion created as a result of ionization of the molecule, its evolution until rescattering, and a nuclear wave packet after rescattering. This complements the three-step model by accounting for what happens with the nuclear subsystem between ionization and rescattering events. A uniform asymptotics defining the PEMDs near a backward rescattering caustic is obtained, which enables one to extract the nuclear wave packet after rescattering from the PEMDs. The theory is illustrated by comparing its predictions with accurate numerical results obtained by solving the TDSE for a one-dimensional molecule with one electronic and one internuclear degree of freedom modeling H_2.

DOI: 10.1103/PhysRevA.104.063115

I. INTRODUCTION

While the theory of ionization of one-electron atoms and molecules with frozen nuclei by intense laser pulses has reached the stage of maturity, with many efficient analytical [1–8] and computational [9–15] methods for studying strong-field phenomena [16] developed, the present understanding of how nuclear motion in molecules affects the ionization dynamics and reveals itself in ionization observables is far less complete. One reason for that is computational: Solving the time-dependent Schrödinger equation (TDSE) numerically, even for the simplest molecular system consisting of one electron and two nuclei with the nuclear motion included, is still not feasible in the three-dimensional case. In this situation, it is natural to resort to the analysis of reduced dimensionality models. Indeed, many calculations for models with one-dimensional [17–25] or two-dimensional [26–34] electron and one internuclear degree of freedom have been reported. Such models often catch the main physics of the process being considered and are helpful for interpreting experiments [35–41]. However, there also exists a gap on the analytical side: Nuclear motion has not been incorporated into the three-step model [42,43], that is, we lack a simple picture of the dynamics supported by an analytical theory which would account for what happens with the nuclei between ionization of a molecule and rescattering of a photoelectron on the molecular ion. In this paper we present such a picture resulting from the adiabatic theory.

In a previous paper [44] we generalized the adiabatic theory of strong-field ionization of one-electron systems with frozen nuclei [8] by including the internuclear motion. We considered a model molecule with one electronic and one internuclear degree of freedom. The adiabatic approximation relies on the presence of different timescales in the system. There are three timescales characterizing the electronic and internuclear motions and the variation of the laser field. Depending on their ratios, two regimes were considered: In one, the field timescale is much larger than that of the electron and nuclei, and in the other, the electronic timescale is much smaller than that of the nuclei and field. Accordingly, two versions of the adiabatic theory were developed. In both cases, the leading-order terms in the asymptotic expansions of the solution to the TDSE and ionization amplitude in the corresponding timescale ratio were obtained. Rescattering, which appears in higher orders of the expansions, was not considered.

Meanwhile, rescattering processes determine the high-energy part of strong-field photoelectron momentum distributions (PEMDs) [45]; therefore, without describing them, the theory initiated in Ref. [44] is not complete. In this paper we extend the theory to include rescattering. This development generalizes the treatment of rescattering in Ref. [8] to the situation where the parent ion on which rescattering of a photoelectron occurs has internal degrees of freedom. We restrict our analysis to the adiabatic regime where the electron is the fastest, which covers current strong-field experiments with lasers operating in the near-infrared range. For real molecules with heavy nuclei, the other regime considered in Ref. [44], where the field is the slowest, belongs to the regime analyzed here. The derivation and the expressions for the rescattering parts of the solution to the TDSE and ionization amplitude obtained involve objects and processes not present in the theory

for systems with fixed nuclei [8]: a nuclear wave packet in the molecular ion created as a result of ionization of the molecule, its evolution until a rescattering event, its transformation due to rescattering, and the resulting nuclear wave packet after rescattering has occurred. All this is described analytically, which fills the gap mentioned above and shows what happens with the nuclear subsystem in strong-field ionization of molecules.

Another aspect of rescattering which attracts much interest in strong-field physics stems from the fact that rescattered photoelectrons imprint information on the structure of the parent ion into the PEMD [46]. Hence, this information can be extracted from experimental PEMDs, which is the essence of rescattering spectroscopy. To establish an extraction procedure, a theory relating the PEMD to the structure information is needed. For systems with frozen nuclei, there exists a well-developed approach based on a factorization formula proposed in Ref. [47]. This formula states that strong-field PEMDs in a region dominated by backward rescattered photoelectrons factorize into the differential cross section (DCS) for elastic scattering of an electron on the potential created by the parent ion and a returning photoelectron wave packet (RWP). It enables one to extract DCSs from experimental PEMDs [48–64]. The factorization formula was derived and an analytical expression for the RWP was obtained within the adiabatic theory [8] in Ref. [65], which made the extraction procedure quantitative [57,60,62,64]. Recently, this theory has been generalized to vortex electrons [15]. In this paper, following Ref. [65], we derive the analog of the factorization formula for the present model including the internuclear motion. The main difference compared to the case of fixed nuclei is that the internuclear motion entangles the ionization and rescattering processes. This essentially modifies the meaning of the factor containing structure information in the factorization formula. We show that it is the nuclear wave packet in the molecular ion *after* rescattering which can be extracted from the PEMD. Having this wave packet and using the theoretical expression for the wave packet *before* rescattering, one can reconstruct the scattering matrix, which is similar to the procedure proposed in Ref. [47]. Alternatively, one can reconstruct the wave packet before rescattering, assuming that the scattering matrix is known, which opens a different avenue for rescattering spectroscopy. Note that the latter wave packet and its evolution in time is what was observed in a pioneering paper [66] and more recently in Refs. [53,63]. The goal of developing the present theory is to describe the nuclear dynamics observed in such experiments and show how a moving nuclear wave packet can be reconstructed from the PEMD.

Since the Keldysh theory [1] and its versions known as the strong-field approximation (SFA) [2,3] are widely used for describing strong-field ionization of systems with fixed nuclei [4–6] and were also applied to systems with moving nuclei [22,31,67], it may be instructive to compare their scope and applicability with that of the adiabatic theory developed in Refs. [8,44] and the present paper. The SFA can be applied for arbitrary frequencies, which is an advantage compared to the adiabatic theory applicable only in the low-frequency case. At the same time, the SFA does not become exact anywhere in the space of parameters defining laser pulse and target properties and, as a consequence, works only qualitatively at best. On the other hand, the adiabatic theory becomes exact in the low-frequency limit and under a certain condition [condition (13) in Ref. [8]; condition (44) given below in the present case] works quantitatively. It is a solid theory of strong-field ionization capable of explaining existing experiments and predicting new strong-field effects; see, e.g., Refs. [15,64,68,69]. A more detailed comparison of the analytical structures of the two approaches can be found in Ref. [8].

The paper is organized as follows. In Sec. II we introduce our model and discuss its properties needed for developing the adiabatic theory. Section III places the model in the time-dependent context and defines ionization observables. Section IV presents the main theoretical results of this paper. In Sec. V the theory is illustrated by calculations for one-cycle pulses. Section VI illustrates the application of the factorization formula for realistic few-cycle pulses with a well-defined carrier-envelope phase (CEP). Section VII summarizes the paper.

II. MODEL

Following Refs. [44,70–73], we consider a model one-dimensional molecule consisting of two identical nuclei with masses $m_1 = m_2 = M$ and charges $q_1 = q_2 = \frac{1}{2}$ and one active electron with mass $m_3 = 1$ and charge $q_3 = -1$ (atomic units used throughout the paper). The molecule is treated in its center-of-mass frame, so the nuclear x_1 and x_2 and electronic x_3 coordinates satisfy $M(x_1 + x_2) + x_3 = 0$. Its Hamiltonian is given by

$$H_0 = -\frac{1}{2\mu}\frac{\partial^2}{\partial R^2} - \frac{1}{2m}\frac{\partial^2}{\partial x^2} + U_{\rm ion}(R) + V(x;R), \qquad (1)$$

where $R = x_2 - x_1$ and $x = x_3 - (x_1 + x_2)/2 = x_3/m$ are Jacobi coordinates and $\mu = M/2$ and $m = 2M/(2M+1)$ are the corresponding reduced masses. The potentials $U_{\rm ion}(R)$ and $V(x;R)$ modeling the internuclear and electron-nuclear interactions, respectively, are defined below. As in our previous paper [44], we assume that the nuclei can neither pass through each other nor move away from each other at an infinite distance, and hence dissociation is not possible. The former assumption reduces the configuration space to the region $0 \leqslant R < \infty$ and $-\infty < x < \infty$. The latter is implemented by using $U_{\rm ion}(R)$ which grows infinitely at $R \to \infty$. Accordingly, all wave functions describing the motion in R involved in the formulation are implied to satisfy zero boundary conditions at $R = 0$ and $R \to \infty$, and we indicate explicitly only the asymptotic boundary conditions at $|x| \to \infty$.

In Ref. [44] we considered models with light ($M \sim 1$) and heavy ($M \gg 1$) nuclei. In the present study, which aims to model H_2, we restrict our treatment to the heavy nuclei case. In this case, the value of m is close to unity. To simplify equations, we set $m = 1$ in the following. Furthermore, the Born-Oppenheimer approximation (BOA) is expected to hold, so we use it below.

A. Potentials

To define the potentials in Eq. (1), we need to formulate the BOA for the present model. Let us consider bound

states of the molecule. The exact bound states are defined by

$$(H_0 - E_n)\Phi_n(x,R) = 0, \tag{2a}$$

$$\Phi_n(x,R)|_{|x|\to\infty} = 0, \tag{2b}$$

where $n = 0, 1, \ldots$ enumerates the states in increasing order of their energy E_n. In the BOA, the solutions to Eqs. (2) are approximated by

$$\Phi_n^{\mathrm{BO}}(x,R) = \Phi_n(R)\phi_e(x;R) \tag{3}$$

and the corresponding energies by E_n^{BO}. Here the electronic wave function is the ground-state solution to (we consider only electronically ground molecular states)

$$\left[-\frac{1}{2}\frac{d^2}{dx^2} + V(x;R) - E_e(R)\right]\phi_e(x;R) = 0, \tag{4a}$$

$$\phi_e(x;R)|_{|x|\to\infty} = 0, \tag{4b}$$

where $E_e(R)$ is the electronic energy. The nuclear wave function and the molecular energy E_n^{BO} are then defined by

$$\left[-\frac{1}{2\mu}\frac{d^2}{dR^2} + U_{\mathrm{mol}}(R) - E_n^{\mathrm{BO}}\right]\Phi_n(R) = 0, \tag{5}$$

where

$$U_{\mathrm{mol}}(R) = U_{\mathrm{ion}}(R) + E_e(R). \tag{6}$$

The functions $\Phi_n(x,R)$, $\Phi_n(R)$, and $\phi_e(x;R)$ are chosen to be real and normalized to unity.

We want the Hamiltonian (1) to model H_2 in the single-active-electron approximation. To this end, $U_{\mathrm{ion}}(R)$ and $U_{\mathrm{mol}}(R)$ should model Born-Oppenheimer (BO) potentials in the ground electronic states of the molecular ion $H_2{}^+$ and neutral molecule H_2, respectively. The potential $U_{\mathrm{ion}}(R)$ is defined by

$$U_{\mathrm{ion}}(R) = \frac{A}{R^2} + B + CR^2, \tag{7}$$

with the parameters $A = 0.26$, $B = -0.732\,635$, and $C = 0.016\,25$. The same internuclear potential was used in Refs. [44,70,71]. The last term in Eq. (7) prevents the molecule from dissociating. With this potential, the molecular ion has a purely discrete spectrum of eigenstates defined by

$$(H_{\mathrm{ion}} - \varepsilon_v)\chi_v(R) = 0, \tag{8}$$

where

$$H_{\mathrm{ion}} = -\frac{1}{2\mu}\frac{d^2}{dR^2} + U_{\mathrm{ion}}(R) \tag{9}$$

and $v = 0, 1, \ldots$ is the vibrational quantum number. The functions $\chi_v(R)$ are real and normalized to unity. The electron-nuclear interaction is modeled by

$$V(x;R) = V\left(x + \frac{R}{2}\right) + V\left(x - \frac{R}{2}\right), \tag{10}$$

where

$$V(x) = -\frac{a_1}{\cosh^2(b_1 x)} - \frac{a_2}{\cosh^2(b_2 x)}, \tag{11}$$

with the parameters $a_1 = 0.8853$, $b_1 = 3.008$, $a_2 = 0.2284$, and $b_2 = 0.4606$. The potential $V(x)$ is similar to the one used in Ref. [44]. We have added the second term in Eq. (11) to make the potential well deeper and thus to increase rescattering. In Fig. 1 the ionic $U_{\mathrm{ion}}(R)$ and molecular $U_{\mathrm{mol}}(R)$ potentials defined above are compared with the BO potentials for $H_2{}^+$ [74] and H_2 [75], respectively. The present model is seen to reproduce the BO potentials for the real systems well near and to the left of their minima at $R_{\mathrm{ion}} = 2$ and $R_{\mathrm{mol}} = 1.4$. In this model, for $M = 1836$ corresponding to H_2, we obtain the exact $E_0 = -1.164\,361$ and BO $E_0^{\mathrm{BO}} = -1.164\,393$ energies of the ground state. These energies differ only in the sixth digit, which shows that the BOA for bound states works rather well. The electronic continuum begins at $\varepsilon_0 = -0.597$, so the ionization potential of the molecule in the ground state is $I_p = \varepsilon_0 - E_0 = 0.568$. The vertical ionization potential at the molecular equilibrium is $U_{\mathrm{ion}}(R_{\mathrm{mol}}) - U_{\mathrm{mol}}(R_{\mathrm{mol}}) = 0.606$.

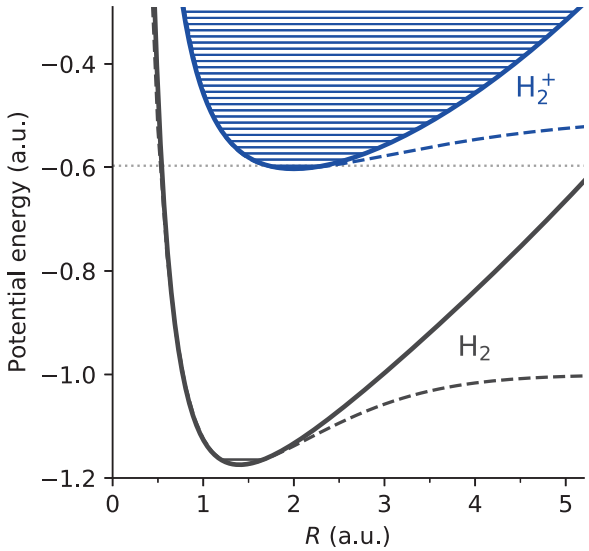

FIG. 1. Upper (blue) and lower (black) solid lines show the ionic $U_{\mathrm{ion}}(R)$ and molecular $U_{\mathrm{mol}}(R)$ potentials in the present model, respectively. The corresponding dashed lines show the BO potentials for real $H_2{}^+$ [74] and H_2 [75]. The ground-state molecular energy E_0 and molecular ion energies ε_v for a number of the lowest vibrational states are shown by horizontal lines superimposed on the corresponding potentials. The horizontal dotted line indicates the boundary of the electronic continuum ε_0

B. Scattering states and scattering matrix

Scattering states of the molecule are needed to define ionization observables. In this section we recall the definition of the exact scattering states and the associated scattering matrix [44] and then discuss how to construct them in the BOA.

The exact *in* (+) and *out* (−) scattering states having an incident wave with momentum k in the entrance vibrational channel v satisfy [44]

$$[H_0 - E_v(k)]\Phi_v^{(\pm)}(x,R;k) = 0, \tag{12}$$

where

$$E_v(k) = \frac{k^2}{2} + \varepsilon_v. \tag{13}$$

We consider these states in the whole range of the incident momentum $-\infty < k < \infty$, with positive and negative k

corresponding to electrons impinging on the molecular ion from the negative and positive ends of the x axis, respectively. The asymptotic boundary conditions for the in states are specified by

$$\Phi_v^{(+)}(x,R;k>0)=\begin{cases}\sum_{v'}\sqrt{\frac{k}{k_{v'}}}e^{ik_{v'}x}\chi_{v'}(R)S^{+}_{v'v}(k), & x\to+\infty\\ e^{ikx}\chi_v(R)-\sum_{v'}\sqrt{\frac{k}{k_{v'}}}e^{-ik_{v'}x}\chi_{v'}(R)S^{-}_{v'v}(k), & x\to-\infty\end{cases} \tag{14a}$$

and

$$\Phi_v^{(+)}(x,R;k<0)=\begin{cases}e^{ikx}\chi_v(R)-\sum_{v'}\sqrt{\frac{|k|}{k_{v'}}}e^{ik_{v'}x}\chi_{v'}(R)S^{+}_{v'v}(k), & x\to+\infty\\ \sum_{v'}\sqrt{\frac{|k|}{k_{v'}}}e^{-ik_{v'}x}\chi_{v'}(R)S^{-}_{v'v}(k), & x\to-\infty,\end{cases} \tag{14b}$$

where $k_{v'}=\sqrt{k^2+2(\varepsilon_v-\varepsilon_{v'})}\geqslant 0$, $S^{\pm}_{v'v}(k)$ is the scattering matrix, its superscript indicates the direction of propagation of the outgoing wave in the exit channel v', and the summations run over all open exit channels with $\varepsilon_{v'}<E_v(k)$. The out states are given in terms of the in states by [76]

$$\Phi_v^{(-)}(x,R;k)=[\Phi_v^{(+)}(x,R;-k)]^*. \tag{15}$$

We have set $m=1$ in these equations as compared to Ref. [44].

For the derivation of the rescattering part of the solution to the TDSE in Sec. IV A, we need an integral representation for the in states. Moving the term with $V(x;R)$ to the right-hand side of Eq. (12), this equation can be cast in the integral form

$$\begin{aligned}&\Phi_v^{(+)}(x,R;k)\\ &\quad=e^{ikx}\chi_v(R)+\int_0^\infty dR'\int_{-\infty}^{\infty}dx'G(x,R,x',R';E_v(k))\\ &\qquad\times V(x';R')\Phi_v^{(+)}(x',R';k),\end{aligned} \tag{16}$$

where

$$G(x,R,x',R';E)=\sum_{v'}G(x-x';E-\varepsilon_{v'})\chi_{v'}(R)\chi_{v'}(R') \tag{17}$$

is the outgoing-wave Green's function for the remaining left-hand side of Eq. (12) and

$$G(x;E)=e^{-3i\pi/4}\int_0^\infty\exp\left(\frac{ix^2}{2t}+iEt\right)\frac{dt}{\sqrt{2\pi t}} \tag{18}$$

is the Green's function describing free motion in x.

The scattering matrix contains information on the structure of the molecule. One of the goals of this paper is to demonstrate how this information can be extracted from ionization observables. To prepare this discussion, here we illustrate the dependence of the scattering matrix on its arguments. For the present homonuclear molecule, the potential (10) is an even function of x. In this case, the scattering matrix satisfies $S^{-}_{v'v}(-k)=S^{+}_{v'v}(k)$, so it is sufficient to consider $S^{+}_{v'v}(k)$. For $k>0$ ($k<0$), the value of $|S^{+}_{v'v}(k)|^2$ gives the probability of transmission (reflection) in the scattering of an electron by the molecular ion accompanied by a vibrational transition $v\to v'$ in the ion. The solid lines in Fig. 2 show such probabilities as functions of k for the entrance channel $v=0$ and exit channels $v'=0$, 1, and 2. One can see that the transmission probability for the vibrationally elastic exit channel $v'=0$ approaches unity as $k>0$ grows, while for inelastic channels $v'>0$ it decays almost monotonically without any pronounced structure. On the other hand, the reflection probabilities for all exit channels demonstrate a regular oscillatory behavior, which is caused by the two-center interference (discussed below), and the envelope of the oscillations decays as $-k>0$ grows. We found that the rate and functional form of this decay depend strongly on the electron-nuclear potential (10). The nearly exponential decay seen in the figure is characteristic of smooth finite-range potentials $V(x)$ of the type used here. In this case, deepening the potential well makes the decay slower.

To simplify the interpretation of the results of the adiabatic theory in the following sections, we need to obtain

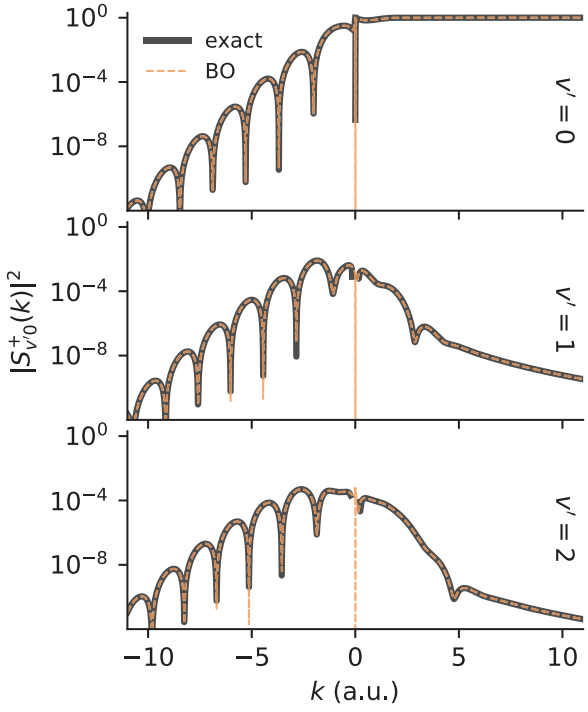

FIG. 2. Transmission ($k>0$) and reflection ($k<0$) probabilities for electron scattering by the molecular ion as functions of the incident momentum k for the entrance channel $v=0$ and exit channels $v'=0$, 1, and 2. Solid (black) lines are obtained using the exact molecular scattering matrix defined by Eqs. (14). Dashed (orange) lines are calculated in the BOA using the scattering matrix from Eq. (22).

a representation for the scattering states and the scattering matrix in the BOA. There exists a well-known problem in constructing molecular scattering states in the BOA. Indeed, within the BOA, the solution to Eq. (12) should be sought in the factorized form similar to Eq. (3), where the electronic wave function is a continuum state in the potential (10) created by fixed nuclei. However, while the electronic energy in a discrete state is a uniquely defined function of R, such as $E_e(R)$ in Eqs. (4), in a continuum state it can arbitrarily depend on R. Since this energy then defines the molecular BO potential in Eq. (5), one can construct infinitely many different BOA representations for the same molecular scattering state. To eliminate this arbitrariness, we adopt an approach proposed in Ref. [77]. In this approach, the electronic energy in a continuum state is assumed to be a constant independent of R. Let us introduce the electronic in scattering states with incident momentum $-\infty < k < \infty$ and energy $k^2/2$ defined by

$$\left[-\frac{1}{2}\frac{d^2}{dx^2} + V(x;R) - \frac{k^2}{2}\right]\phi_e^{(+)}(x;R,k) = 0 \tag{19}$$

subject to the boundary conditions

$$\phi_e^{(+)}(x;R,k>0) = \begin{cases} e^{ikx}S^+(k;R), & x \to +\infty \\ e^{ikx} - e^{-ikx}S^-(k;R), & x \to -\infty \end{cases} \tag{20a}$$

and

$$\phi_e^{(+)}(x;R,k<0) = \begin{cases} e^{ikx} - e^{-ikx}S^+(k;R), & x \to +\infty \\ e^{ikx}S^-(k;R), & x \to -\infty. \end{cases} \tag{20b}$$

Here $S^{\pm}(k;R)$ is the electronic scattering matrix which depends on R as a parameter and its superscript again indicates the direction of propagation of the scattered wave. Then the in solutions to Eq. (12) in the BOA can be approximated by

$$\Phi_v^{(+)\mathrm{BO}}(x,R;k) = \chi_v(R)\phi_e^{(+)}(x;R,k). \tag{21}$$

We mention that a similar approximation based on the approach introduced in Ref. [77] was used in Ref. [22] to describe double continuum molecular scattering states in the analysis of strong-field ionization happening simultaneously with dissociation of the molecule. The scattering matrix can be found by comparing Eqs. (20) and (21) with Eqs. (14). Note that $\varepsilon_v - \varepsilon_{v'} = O(M^{-1/2})$, and hence within the BOA one should substitute $k_{v'} \approx |k|$ into Eqs. (14). We thus obtain

$$S_{v'v}^{\pm,\mathrm{BO}}(k) = \int_0^\infty \chi_{v'}(R)S^{\pm}(k;R)\chi_v(R)dR, \tag{22}$$

which is the BOA for $S_{v'v}^{\pm}(k)$.

Let us illustrate the quantitative performance of this approximation. We first discuss the electronic scattering matrix. For the present model it satisfies $S^-(-k;R) = S^+(k;R)$, so it is sufficient to consider $S^+(k;R)$. The value of $|S^+(k;R)|^2$ gives the probability of reflection ($k < 0$) or transmission ($k > 0$) in the scattering of an electron by the potential $V(x;R)$. These probabilities as functions of k and R are shown in Fig. 3. For any fixed R, the transmission probability quickly approaches unity as $k > 0$ grows. The reflection probability oscillates with a decaying envelope as $-k > 0$ grows, which is similar to the behavior seen at $k < 0$ in Fig. 2. For the present one-dimensional scattering, the minima of the oscillations in

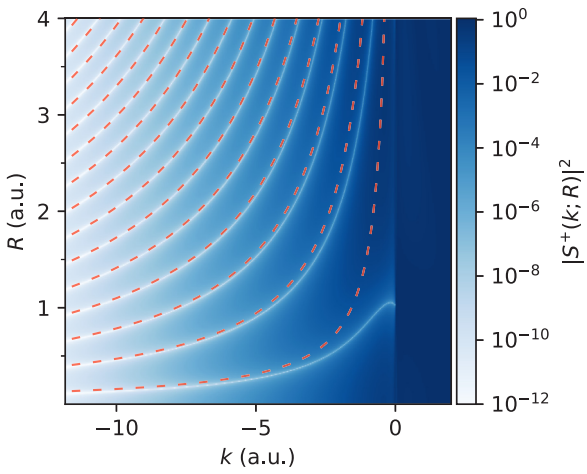

FIG. 3. Transmission ($k > 0$) and reflection ($k < 0$) probabilities for electron scattering by fixed nuclei as functions of the incident momentum k and internuclear distance R. White lines indicate nodal lines of the electronic scattering matrix $S^+(k;R)$. Dashed lines are obtained from Eq. (23).

k indicate zeros of $S^+(k;R)$. The positions of the zeros depend on R, which forms nodal lines seen as white lines at $k < 0$ in Fig. 3. Dashed lines in Fig. 2 are obtained using the molecular scattering matrix in the BOA from Eq. (22). The good agreement with the exact results confirms the validity of the present BOA for scattering states. Some difference between the results can be seen near $k = 0$, which is expectable, since we have neglected $\varepsilon_v - \varepsilon_{v'}$ compared to k^2 in arriving at Eq. (22).

Having demonstrated that Eq. (22) works well, the behavior of $S_{v'v}^{+}(k)$ can be understood in terms of that of the simpler object $S^+(k;R)$. Let us return to the oscillatory structure at $k < 0$ in Fig. 2. We have already stated that it is caused by the two-center interference. Now we can quantify the statement. We employ the simplest model in which an electron is reflected either at $x = -R/2$ or at $x = R/2$. The requirement that the two reflected waves interfere destructively reads

$$2|k|R = \pi(2n+1), \quad n = 0, 1, \ldots. \tag{23}$$

Thus, one can expect that the reflection probability turns to zero when the condition (23) is fulfilled. This happens along the dashed lines in Fig. 3. These lines indeed approximately reproduce nodal lines of $S^+(k;R)$, and at larger $|k|$ the approximation works better. This means that $S^+(k;R)$ oscillates as a function of R at a given $k < 0$, and the phase of these oscillations depends on k. The product of the molecular ion states in the integrand in Eq. (22) is localized near the minimum of $U_{\mathrm{ion}}(R)$ and serves as a window function. As k varies, the integral oscillates approximately as $S^+(k;R_{\mathrm{ion}})$, which explains the oscillations seen in Fig. 2. Note that there is some phase shift between the oscillations for different v', which is caused by finiteness of the width of ionic states.

C. Electronic Siegert states

Within the adiabatic theory, ionization observables in a strong laser field are expressed in terms of appropriate Siegert states (SSs) in a static electric field [8,44]. In the presence of an external static electric field F, the Hamiltonian of the

molecule in the present model is $H_0 + Fx$. The molecular SSs are the eigenfunctions of this Hamiltonian satisfying outgoing-wave boundary conditions [44,70–73]. The electronic SSs appear naturally when the molecular SSs are described in the BOA [44]. For the present study, we need only one electronic SS which originates from the ground electronic state defined by Eq. (4) as the field is turned on. In this section we recall its definition and illustrate its properties.

The electronic SSs are the solutions to [44]

$$\left[-\frac{1}{2}\frac{d^2}{dx^2} + V(x;R) + Fx - E_e(R,F)\right]\phi_e(x;R,F) = 0 \tag{24}$$

subject to the outgoing-wave boundary conditions

$$\phi_e(x;R,F) = \begin{cases} f(R,F)e(x,E(R,F)), & x \to -s\infty \\ 0, & x \to +s\infty, \end{cases} \tag{25}$$

where $s = \mathrm{sgn}(F)$ and

$$e(x,E) = \frac{1}{|2Fx|^{1/4}} \exp\left[i\frac{2^{1/2}}{|F|}\left(\frac{2}{3}|Fx|^{3/2} + E|Fx|^{1/2}\right)\right]. \tag{26}$$

This is an eigenvalue problem, it has an infinite discrete set of solutions which depend on R and F as parameters. We are interested in the SS satisfying

$$E_e(R,F)|_{|F|\to 0} = E_e(R), \quad \phi_e(x;R,F)|_{|F|\to 0} = \phi_e(x;R). \tag{27}$$

The SS eigenvalue is complex and can be presented in the form

$$E_e(R,F) = \mathcal{E}_e(R,F) - \frac{i}{2}\Gamma_e(R,F), \tag{28}$$

which defines the Stark-shifted energy $\mathcal{E}_e(R,F)$ and ionization rate $\Gamma_e(R,F)$ of the electronic state. The dependence of these functions on R and F in the present model is illustrated in Fig. 4. The SS eigenfunction is also complex and normalized by

$$\int_{-\infty}^{\infty} \phi_e^2(x;R,F)dx = 1 \tag{29}$$

without complex conjugation. In the weak-field limit, the rate is related to the ionization amplitude $f(R,F)$ appearing in Eq. (25),

$$\Gamma_e(R,F)_{|F|\to 0} = |f(R,F)|^2. \tag{30}$$

The functions $E_e(R,F)$ and $f(R,F)$ are needed for implementing the adiabatic theory in the heavy nuclei case [44].

To close Sec. II introducing our model, let us summarize and partially justify its main simplifications compared to real molecules. First, we consider a system with only one electronic and one nuclear degree of freedom. The reason for this is that to validate our theory we need accurate numerical results obtained by solving the TDSE, but this is not feasible in the three-dimensional case. Note that all previous studies including the internuclear motion [17–41] also treated reduced dimensionality models. We mention that there exists a powerful method for calculating three-dimensional electronic SSs developed in Refs. [78,79], so the theory initiated in Ref. [44] and extended below can be implemented for a three-dimensional electron. Second, the electron-nuclear interaction is modeled by a finite-range potential (11). Note that the Keldysh theory [1] and the SFA [2,3] were originally formulated also for finite-range potentials. Corrections caused by the Coulomb tail of the interaction were included in these theories later (see, e.g., Ref. [80]) and can be similarly included in the adiabatic theory. Third, dissociation is not possible in the present model. It was shown that the probability of dissociation at field strengths of interest in strong-field physics is rather small [72,73]. Yet including the dissociation channel along with vibrational excitation accounted for here is one of the most interesting directions for future studies. Despite all these simplifications, the present model reproduces the major effect of the internuclear motion on the dynamics of tunneling (or over-the-barrier) ionization, as discussed in Ref. [44], and rescattering, as shown below, and this effect is worth studying.

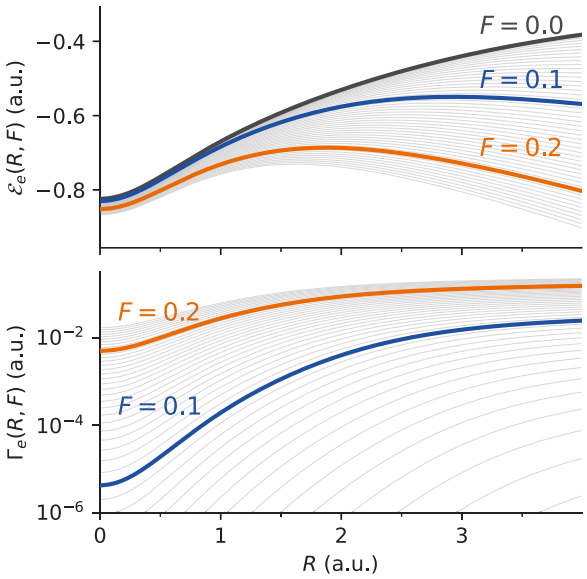

FIG. 4. Energy $\mathcal{E}_e(R,F)$ and ionization rate $\Gamma_e(R,F)$ for the electronic SS originating from the ground electronic state as functions of R at a fixed F. The thin (gray) lines show the results for F from 0 to 0.25 in steps of 0.005. The results for $F = 0.0$, 0.1, and 0.2 are highlighted by thick (colored) lines.

III. TIME-DEPENDENT SCHRÖDINGER EQUATION AND OBSERVABLES

The TDSE describing the molecule interacting with a laser pulse in the dipole approximation and length gauge reads [44]

$$i\frac{\partial}{\partial t}\Psi(x,R,t) = [H_0 + F(t)x]\Psi(x,R,t). \tag{31}$$

Here $F(t)$ is the electric field of the pulse satisfying $F(t \to \pm\infty) = 0$. We assume that the molecule is initially in its ground state defined by Eq. (2) with $n = 0$. This leads to the initial condition

$$\Psi(x,R,t \to -\infty) = \Phi_0(x,R)e^{-iE_0 t}. \tag{32}$$

As a result of the interaction, the molecule can be ionized. All ionization observables can be expressed in terms of the

ionization amplitude

$$I_v(k) = e^{iE_v(k)t} \int_0^\infty dR \int_{-\infty}^\infty dx\, \Phi_v^{(-)*}(x, R; k)\Psi(x, R, t)\Big|_{t\to\infty}. \tag{33}$$

Thus, the partial PEMD describing the ionization process in which an electron flies away with asymptotic momentum k while the molecular ion is left in vibrational state v is given by

$$P_v(k) = |I_v(k)|^2. \tag{34}$$

This is the most detailed characteristic of ionization from which other ionization observables can be obtained by summing over v and/or integrating over k [44].

To develop the adiabatic theory, it is convenient to rewrite these equations in alternative forms. The TDSE (31) can be presented in the integral form [44]

$$\Psi(x, R, t) = i \int_{-\infty}^t dt' \int_0^\infty dR' \int_{-\infty}^\infty dx' G_x(x, t; x', t') \times G_R(R, R', t - t')V(x'; R')\Psi(x', R', t'). \tag{35}$$

Here the electronic Green's function is given by [81]

$$G_x(x, t; x', t') = \theta(t - t')\frac{e^{-3i\pi/4}}{\sqrt{2\pi(t - t')}} e^{i\mathcal{S}(x,t;x',t')}, \tag{36}$$

where $\mathcal{S}(x, t; x', t')$ is the classical action accumulated along a trajectory connecting the space-time points (x', t') and (x, t). Let us introduce a reference trajectory with the velocity $v(t)$ and coordinate $x(t)$ defined by

$$\dot v(t) = -F(t), \quad \dot x(t) = v(t), \tag{37a}$$

$$v(t \to -\infty) = x(t \to -\infty) = 0. \tag{37b}$$

Then the action in Eq. (36) is given by [8]

$$\mathcal{S}(x, t; x', t') = v(t)x - v(t')x' + \frac{[x(t) - x(t') - (x - x')]^2}{2(t - t')} - \frac{1}{2}\int_{t'}^t v^2(t'')dt''. \tag{38}$$

The nuclear Green's function in Eq. (35) can be expanded in eigenstates of the molecular ion defined by Eq. (8),

$$G_R(R, R', t) = -i\theta(t)\sum_v e^{-i\varepsilon_v t}\chi_v(R)\chi_v(R'). \tag{39}$$

The ionization amplitude (33) can be presented as [44]

$$I_v(k) = \int_{-\infty}^\infty dt \int_0^\infty dR\, e^{i\varepsilon_v t}\chi_v(R)[j(x \to \infty, R, t) - j(x \to -\infty, R, t)], \tag{40}$$

where

$$j(x, R, t) = -\frac{i}{2}\left[e^{-i\mathcal{S}(x,t;k)}\frac{\partial}{\partial x}\Psi(x, R, t) - \Psi(x, R, t)\frac{\partial}{\partial x}e^{-i\mathcal{S}(x,t;k)}\right] \tag{41}$$

is the ionization flux and $\mathcal{S}(x, t; k)$ is the classical action for a trajectory passing through the point (x, t) and having the asymptotic momentum k. This action is given by [8]

$$\mathcal{S}(x, t; k) = u_i(t, k)x - \mathcal{S}(t; k), \tag{42a}$$

$$\mathcal{S}(t; k) = \frac{k^2 t}{2} - \frac{1}{2}\int_t^\infty [u_i^2(t', k) - k^2]dt', \tag{42b}$$

where $u_i(t, k)$ is the initial velocity of the trajectory at time t,

$$u_i(t, k) = k - v_\infty + v(t), \tag{43}$$

and $v_\infty = v(t \to \infty)$.

IV. ADIABATIC THEORY

Let T_e, T_n, and T_f denote timescales characterizing the electronic and internuclear motions in the molecule and variation of the laser field, respectively. In Ref. [44], two versions of the adiabatic theory applicable in the different ranges of these timescales were developed. In this paper we assume that the electron is the fastest, that is,

$$T_e \ll \min(T_n, T_f). \tag{44}$$

This version of the theory is called the adiabatic approximation for slow nuclei and field (AAnf). For real molecules $T_e \ll T_n$, so the condition (44) amounts to $T_e \ll T_f$. Note, importantly, that this condition implies no assumption regarding the relation between T_n and T_f. The timescales can be estimated as $T_e = 2\pi/I_p$, $T_n = 2\pi/\Delta E_n$, and $T_f = 2\pi/\omega$, where I_p is the ionization potential of the molecule, ΔE_n is the energy difference between its ground and first exited vibrational states, and ω is the laser frequency. For H_2 at a wavelength of 800 nm, we obtain $T_e = 11$, $T_n = 331$ [82], and $T_f = 110$. Thus, the AAnf covers current experiments on strong-field ionization of molecules with lasers operating in the near-infrared range and remains applicable at all longer wavelengths. The other version of the theory called the adiabatic approximation for a slow field (AAf) applies when the field is the slowest, that is, $\max(T_e, T_n) \ll T_f$. In contrast to the AAnf, it allows one to treat models with light nuclei, when $T_e \sim T_n$. For real molecules with heavy nuclei, it becomes applicable at much longer wavelengths satisfying $T_n \ll T_f$. In this case, however, the condition (44) is fulfilled, and hence the AAf reduces to the AAnf [44].

Let us introduce timescale ratios $\epsilon_n = T_e/T_n$ and $\epsilon_f = T_e/T_f$ characterizing adiabaticity of the internuclear motion and variation of the field, respectively. The applicability of the AAnf is controlled by the parameter [44]

$$\epsilon_{nf} = \max(\epsilon_n, \epsilon_f). \tag{45}$$

In the AAnf, the solution to the TDSE (31) and the ionization amplitude (33) are sought as the asymptotic expansions in ϵ_{nf} for $\epsilon_{nf} \to 0$. Note that this implies the limit $M \to \infty$, so we continue to use the BOA in the time-dependent context below. The expansions consist of adiabatic and rescattering parts which should be treated separately. The adiabatic parts of the wave function and ionization amplitude were obtained in Ref. [44]. In Secs. IV A and IV B we recall these results and derive the corresponding rescattering parts. The asymptotics presented in these sections are obtained in the leading order in

ϵ_{nf} and are therefore called *simple*. In Sec. IV C we obtain a *uniform* asymptotics describing backward rescattering near a caustic. In Sec. IV D we simplify the results by expressing the scattering state and scattering matrix defining the asymptotics of rescattering parts in the BOA.

A. Wave function

In the limit $\epsilon_f \to 0$, the solution to Eqs. (31) and (32) can be presented as a sum of adiabatic and rescattering parts [8],

$$\Psi(x,R,t) = \Psi_a(x,R,t) + \Psi_r(x,R,t). \tag{46}$$

The adiabatic part $\Psi_a(x,R,t)$ describes a state in which the electron remains quasibound, continuously adjusting to the instantaneous value of the laser field $F(t)$. The leakage of electrons in this state results in ionization of the molecule. The rescattering part $\Psi_r(x,R,t)$ describes recollision which occurs when an electron liberated from the molecule returns to the molecular ion. The two terms in Eq. (46) differ by their amplitudes, which scale as $O(\epsilon_f^0)$ and $O(\epsilon_f^{1/2})$, and phases, which scale as $O(\epsilon_f^{-1})$ and $O(\epsilon_f^{-3})$, respectively. These estimates involve only ϵ_f and do not depend on ϵ_n because the dynamics of an electron between its liberation and rescattering is fully determined by the electron-field interaction. Equation (46) holds within a quasistationary zone $|x| \ll X_f$, where $X_f = F_0 T_f^2 = O(\epsilon_f^{-2})$ and F_0 is the characteristic value of $|F(t)|$ [8]. In this zone the electron-field interaction can be treated as if the field were static. At the same time, the BOA used below in the presence of a static electric field F_0 holds in the region $|x| \ll X_n$, where $X_n = F_0 T_n^2 = O(\epsilon_n^{-2})$ [70]. Thus, in this section we construct the wave function in the form (46), restricting our treatment to the region $|x| \ll \min(X_n, X_f) = O(\epsilon_{nf}^{-2})$. This is sufficient for calculating the ionization amplitude in the next section.

The leading-order term in the asymptotics of the adiabatic part in Eq. (46) for $\epsilon_{nf} \to 0$ obtained in Ref. [44] is given by

$$\Psi_a(x,R,t) = \Psi(R,t)\phi_e(x;R,F(t)). \tag{47}$$

Such a factorization into nuclear and electronic wave functions, where the latter depends parametrically on the internuclear distance R, results from the BOA, as in Eqs. (3) and (21). The electronic factor in Eq. (47) is the electronic SS defined by Eqs. (24)–(27). It additionally depends parametrically on the field strength F, which makes it a slow function of time varying with timescale T_f. The nuclear factor is the solution to the nuclear TDSE

$$i\frac{\partial}{\partial t}\Psi(R,t) = \left[-\frac{1}{2\mu}\frac{\partial^2}{\partial R^2} + U_{\rm mol}(R,F(t))\right]\Psi(R,t), \tag{48a}$$

$$\Psi(R,t\to-\infty) = \Phi_0(R)e^{-iE_0^{\rm BO}t}, \tag{48b}$$

where

$$U_{\rm mol}(R,F) = U_{\rm ion}(R) + E_e(R,F). \tag{49}$$

The potential in Eq. (48a) depends on t, which causes vibrational excitation of the molecule. Only a finite number of excited states can be appreciably populated during the pulse. This means that $e^{iE_0^{\rm BO}t}\Psi(R,t)$ is a slow function of time varying with timescale T_n. The nuclear TDSE should be solved without any further approximations since the ratio of T_f and T_n can be arbitrary. Note that the evolution described by this equation does not preserve the norm of $\Psi(R,t)$, because the electronic energy in Eq. (49) is complex. Its imaginary part is negative [see Eq. (28)], so the norm decays with time, which accounts for depletion of the adiabatic part (47) caused by ionization of the molecule.

We now derive the rescattering part in Eq. (46). The derivation follows that in Ref. [8]. We only outline its main steps, omitting details thoroughly discussed in Ref. [8].

The derivation is based on Eq. (35). In the limit $\epsilon_f \to 0$, the integral over t' in this equation can be calculated using the saddle point (SP) method. The corresponding SPs can be divided into two groups: (i) a complex consisting of two *adiabatic* and two *tunneling* SPs located near $t' = t$ in the adiabatic zone A defined by $|t'-t| \ll T_f$ and (ii) isolated *rescattering* SPs located at a large distance $|t'-t| \sim T_f = O(\epsilon_f^{-1})$ from $t' = t$ and each other. The two groups can be treated independently and contribute additively to the integral, which explains the two terms in Eq. (46). The adiabatic part (47) represents the contribution from the complex of four SPs in zone A. The rescattering part is a sum of contributions from rescattering SPs. Its derivation proceeds in two stages.

In the first stage, we substitute Eq. (47) for the wave function into the right-hand side of Eq. (35). The contribution to the integral over t' from zone A should be excluded, since it is already included in the adiabatic part on the left-hand side of the equation. We thus obtain a function

$$\Psi_r^{(a)}(x,R,t) = \sum_v \Psi_{r,v}^{(a)}(x,t)\chi_v(R), \tag{50}$$

where

$$\begin{aligned}\Psi_{r,v}^{(a)}(x,t) = \frac{e^{-3i\pi/4}}{\sqrt{2\pi}}\int_{-\infty}^{t}\Bigg[\int_0^\infty dR'\chi_v(R') \\ \times\int_{-\infty}^{\infty}dx' e^{i\mathcal{S}(x,t;x',t')-i\varepsilon_v(t-t')} \\ \times V(x';R')\Psi(R',t')\phi_e(x';R',F(t'))\Bigg] \\ \times\left.\frac{dt'}{\sqrt{t-t'}}\right|_{t'\notin A}.\end{aligned} \tag{51}$$

This expression can be essentially simplified. First, we substitute $V(x;R)\phi_e(x;R,F)$ from Eq. (24) and integrate over x' by parts using Eq. (25). Then we calculate the integral over t'. The condition $t' \notin A$ in Eq. (51) means that only contributions from rescattering SPs should be taken into account. Each such SP is associated with a closed rescattering trajectory (CRT) [83]. A trajectory of an electron driven by the field $F(t)$ is closed if it begins and ends at the same spatial point. The initial and final velocities of a closed trajectory which begins and ends at times t' and t, respectively, can be expressed in terms of the reference trajectory defined by

Eqs. (37),

$$u_i(t,t') = v(t') - \frac{x(t)-x(t')}{t-t'}, \tag{52a}$$

$$u_f(t,t') = v(t) - \frac{x(t)-x(t')}{t-t'}. \tag{52b}$$

The action accumulated along a closed trajectory is $\mathcal{S}(t,t') = \mathcal{S}(0,t;0,t')$. For the time being, we define a CRT as a closed trajectory for which

$$u_i(t,t') = 0 \to t' = t_i(t). \tag{53}$$

For the following, we need the derivative

$$\frac{dt_i(t)}{dt} = \frac{-u_f(t)}{(t-t_i)F(t_i)}, \tag{54}$$

where

$$u_f(t) = u_f(t,t_i) = v(t) - v(t_i) \tag{55}$$

is the final velocity of the CRT. The solutions to Eq. (53) have the meaning of ionization times for electrons which experience rescattering at a given time t. They constitute the set of rescattering SPs contributing to the integral over t' in Eq. (51). Calculating the integral by the SP method, we obtain

$$\Psi^{(a)}_{r,v}(x,t) = \sum_i \frac{g_v(t_i)}{|(t-t_i)F(t_i)|^{1/2}} \exp[iu_f(t)x + i\mathcal{S}(t,t_i) - i\varepsilon_v(t-t_i)], \tag{56}$$

where

$$g_v(t) = \int_0^\infty \chi_v(R) f(R, F(t)) \Psi(R,t) dR \tag{57}$$

and the summation runs over the different solutions to Eq. (53). The term $\mathcal{S}(t,t_i)$ in the exponent is the classical action accumulated along the corresponding CRT. For rescattering SPs $|t-t_i| = O(\epsilon_f^{-1})$; hence $\mathcal{S}(t,t_i) = O(\epsilon_f^{-3})$. This action causes the fastest dependence in Eq. (56) on t.

The second stage of the derivation begins by noting the following. The function $\Psi^{(a)}_r(x,R,t)$ constructed above gives a contribution to the rescattering part $\Psi_r(x,R,t)$ of the wave function. There exist, however, other contributions with the same fast dependence on t. Indeed, substituting Eqs. (50) and (56) into the right-hand side of Eq. (35) and calculating the contribution from the adiabatic zone A, one obtains a function similar to $\Psi^{(a)}_r(x,R,t)$ given by a sum over i of terms with the same actions $\mathcal{S}(t,t_i)$ but different amplitudes. This function also contributes to $\Psi_r(x,R,t)$. Substituting it into Eq. (35) and again calculating the contribution from zone A, one obtains yet another contribution to $\Psi_r(x,R,t)$ with the same actions, etc. This consideration suggests that $\Psi_r(x,R,t)$ satisfies the inhomogeneous integral equation

$$\Psi_r(x,R,t) = \Psi^{(a)}_r(x,R,t) + i\int_{-\infty}^{t} \times \left[\int_0^\infty dR' \int_{-\infty}^\infty dx' G_x(x,t;x',t') \times G_R(R,R',t-t')V(x';R')\Psi_r(x',R',t')\right] dt'\Big|_{t'\in A}, \tag{58}$$

where $\Psi^{(a)}_r(x,R,t)$ acts as a source term. We seek its solution in the form

$$\Psi_r(x,R,t) = \sum_i \sum_v \frac{g_v(t_i)}{|(t-t_i)F(t_i)|^{1/2}} \psi_v(x,R,t) \times \exp[i\mathcal{S}(t,t_i) - i\varepsilon_v(t-t_i)], \tag{59}$$

where the function $\psi_v(x,R,t)$ is to be found. Inserting this into Eq. (58) and calculating the integral over t' using Eqs. (17) and (18), we obtain

$$\psi_v(x,R,t) = \chi_v(R)e^{iu_f(t)x} + \int_0^\infty dR' \int_{-\infty}^\infty dx' \times G\left(x,R,x',R';\tfrac{1}{2}u_f^2(t)+\varepsilon_v\right) \times V(x';R')\psi_v(x',R',t). \tag{60}$$

Comparing this equation with Eq. (16), we find

$$\psi_v(x,R,t) = \Phi^{(+)}_v(x,R;u_f(t)). \tag{61}$$

Summarizing, the leading-order term in the asymptotics of the rescattering part of the wave function for $\epsilon_{nf} \to 0$ is given by

$$\Psi_r(x,R,t) = \sum_i \sum_v \frac{g_v(t_i)}{|(t-t_i)F(t_i)|^{1/2}} \Phi^{(+)}_v(x,R;u_f(t)) \times \exp[i\mathcal{S}(t,t_i) - i\varepsilon_v(t-t_i)], \tag{62}$$

where $t_i = t_i(t)$ is defined by Eq. (53). This result has a transparent interpretation [83]. The sum over i presents independent contributions from the different rescattering SPs. The following physical picture underlies each such contribution. The molecule survives in the state (47) until time t_i. Then it is ionized, and the sum over v accounts for the different ionization channels. The factor $g_v(t_i)$ gives the amplitude of ionization with the molecular ion left in state v. The exponential factor includes the classical action $\mathcal{S}(t,t_i)$ accumulated by the liberated electron and the quantum action $-\varepsilon_v(t-t_i)$ accumulated by the ion as the electron travels along the CRT. At time t, the electron arrives for rescattering as a plane wave with incident momentum $u_f(t)$, while the ion remains in state v. This intermediate state of the system is described by the first term on the right-hand side of Eq. (60). The number of electrons liberated into channel v during the interval dt_i is $|g_v(t_i)|^2|dt_i|$. These electrons undergo rescattering during an interval dt related to dt_i by Eq. (54). Thus the flux in the plane wave arriving for rescattering is $|g_v(t_i)|^2|dt_i/dt|$. The first factor in Eq. (62) is then seen to give the amplitude of the plane wave. As a result of the electron-ion interaction, the incident plane wave in channel v turns into the exact molecular scattering state with the same incident momentum $u_f(t)$, which completes the rescattering process.

Equation (62) is obtained by substituting Eq. (47) for the wave function into the right-hand side of Eq. (35). As is clear from the picture discussed above, it accounts for only one rescattering event. Substituting Eq. (62) for the wave function into the right-hand side of Eq. (35) and repeating the derivation, we would obtain a contribution to the rescattering part in Eq. (46) which accounts for two rescattering events, etc. We restrict our treatment to one-rescattering processes. However, it is instructive to outline the general structure of $\Psi_r(x,R,t)$ which would be obtained by including multiple rescatterings.

To this end, we need to extend the definition of the CRT [83]. A closed trajectory which begins and ends at $x = 0$ and does not pass through this point in between is called a loop. Two loops are said to be connected by a rescattering event if the second loop begins when the first one ends and its initial velocity is either equal (transmission) or opposite (reflection) to the final velocity of the first loop. In the time-dependent context, transmission and reflection are also referred to as forward and backward rescattering, respectively. A general CRT consists of several loops connected by rescattering events, with the first loop having zero initial velocity. Closed rescattering trajectories are characterized by the number of loops L and signature $\Sigma' = \sigma_1 \dots \sigma_{L-1}$, where each symbol σ_l, $l = 1, \dots, L-1$, is either plus or minus, depending on whether the corresponding rescattering event results in transmission or reflection, respectively. For one-loop CRTs the signature Σ' is empty. Closed rescattering trajectories whose signature consists only of pluses are called transmission CRTs. A transmission CRT is a finite piece of a single classical trajectory; its initial and final times satisfy Eq. (53). Thus the CRTs defined by Eq. (53) are particular members of the set of all CRTs for a given t. The role of CRTs in the present discussion stems from the fact that each of them produces a contribution to the asymptotics of $\Psi_r(x, R, t)$ for $\epsilon_f \to 0$. Equation (62) correctly accounts only for contributions from one-loop CRTs, it approximately accounts for contributions from multiloop ($L > 1$) transmission CRTs, treating correctly only one rescattering event at the end of the CRT and neglecting the electron-ion interaction in all intermediate transmissions, and it does not account for contributions from CRTs containing reflections. In the adiabatic regime, the incident velocity of an electron arriving for rescattering is $O(\epsilon_f^{-1})$, so reflection and inelastic transmission processes are suppressed (see Fig. 2). This justifies the approximation in treating contributions from multiloop transmission CRTs and neglecting contributions from CRTs containing reflections. Thus, Eq. (62) indeed gives the leading-order term in the asymptotics of $\Psi_r(x, R, t)$ for $\epsilon_f \to 0$. Higher-order contributions to the rescattering part of the wave function from multiloop CRTs in the zero-range-potential model were analyzed in Ref. [83].

B. Ionization amplitude

Let us turn to the calculation of the ionization amplitude (33). It is linear in the wave function and hence can be also presented as a sum of adiabatic and rescattering parts [8]

$$I_v(k) = I_{v,a}(k) + I_{v,r}(k), \tag{63}$$

corresponding to the two terms in Eq. (46), respectively. The calculation of $I_v(k)$ is based on Eq. (40). Let a denote the maximum range of the electron-nuclear potential $V(x; R)$ in x for the interval of internuclear distances R involved in the ionization dynamics. Then one can replace $x \to \pm\infty$ by $x = \pm a$ in the first argument of the fluxes in Eq. (40) [44]. Thus to calculate $I_v(k)$ it is sufficient to know the wave function in the region $|x| \lesssim a = O(\epsilon_{nf}^0)$, where the asymptotics obtained in the preceding section hold.

Before proceeding, let us note the following. The separation of the ionization amplitude into adiabatic and rescattering parts in Eq. (63) is a consequence of Eq. (46). The two terms in Eq. (46) in turn are distinguished within the adiabatic theory by the behavior of their amplitudes and phases as the adiabatic parameter ϵ_f tends to zero, as discussed below Eq. (46). In fact, recognizing the difference between the adiabatic and rescattering parts of the wave function in Eq. (46) is the essence of the adiabatic theory developed in Refs. [8,44] and the present paper. A somewhat similar separation of the ionization amplitude into direct and rescattering parts is discussed within the SFA (see, e.g., Refs. [80,84]). In this case, however, the direct part originates from the unperturbed initial bound state in which the interaction with the ionizing laser field is neglected, while the adiabatic part of the wave function in the present theory [Eq. (47)] fully incorporates the interaction with the instantaneous field. Furthermore, the rescattering part in the SFA accounts for the interaction with the target potential only within the Born approximation, while in the adiabatic theory the exact scattering state appears in the rescattering part of the wave function [Eq. (62)]. Thus, the similarity between the two theories is limited.

The adiabatic part in Eq. (63) is obtained by substituting Eq. (47) into Eq. (41) and calculating the integral over t in Eq. (40) by the SP method [44]. The corresponding SPs are associated with ionizing rescattering trajectories (IRTs) [83]. In the general case, an IRT consists of a CRT connected by a rescattering event with a semi-infinite trajectory which never passes through $x = 0$. Ionizing rescattering trajectories are characterized by the number of loops L in the CRT and signature $\Sigma = \Sigma'\sigma_L$, where Σ' is the signature of the CRT and $\sigma_L = \pm$ specifies the result of the last rescattering event. For zero-loop IRTs the signature Σ is empty. The SPs contributing to $I_{v,a}(k)$ are associated with transmission IRTs for which Σ either is empty or contains only pluses. It is convenient to introduce reduced signature $\bar{\Sigma}$ which is obtained from Σ by omitting all trailing pluses. For transmission IRTs $\bar{\Sigma}$ is empty. A transmission IRT is a semi-infinite piece of a single classical trajectory. The initial velocity of a trajectory with asymptotic momentum k is given by Eq. (43). Thus the ionization time of a transmission IRT for a given k is defined by

$$u_i(t, k) = 0 \to t = t_i(k). \tag{64}$$

The SPs we need are the solutions to this equation. The leading-order term in the asymptotics of $I_{v,a}(k)$ for $\epsilon_{nf} \to 0$ obtained in Ref. [44] is given by

$$I_{v,a}(k) = e^{i\pi/4}(2\pi)^{1/2} \sum_i \frac{g_v(t_i)}{|F(t_i)|^{1/2}} \exp[i\mathcal{S}(t_i; k) + i\varepsilon_v t_i], \tag{65}$$

where $t_i = t_i(k)$ and the summation runs over the different solutions to Eq. (64).

As is clear from this discussion, the adiabatic part in Eq. (63) accounts only for contributions from transmission IRTs. Such IRTs containing one or more loops pass through the origin, where electron-ion interaction takes place. However, Eq. (65) does not take this interaction into account. The rescattering part in Eq. (63) corrects this drawback of Eq. (65) and in addition accounts for contributions from IRTs containing reflections.

We now derive the rescattering part, again following Ref. [8] and omitting technical details. To do this, we substitute Eq. (62) into Eq. (41). The corresponding SPs for the

integral over t in Eq. (40) are associated with IRTs having asymptotic momentum k and such that all signs in their signatures are pluses except one, which may be either plus or minus. They are defined by

$$u_i(t,k) = \sigma u_f(t) \to t = t_r^\sigma(k), \tag{66}$$

where $\sigma = \pm$ is the sign characterizing the selected rescattering event. The solutions to Eq. (66) have the meaning of time when this rescattering occurs. Note that $u_f(t)$ defined by Eq. (55) implicitly depends on the index i identifying the particular solution to Eq. (53), and hence so does $t_r^\sigma(k)$, while r enumerates the different solutions for given i and σ. Calculating the contributions from these SPs and noting that at $|x| \gtrsim a$ the scattering state in Eq. (62) can be substituted by its asymptotics given by Eqs. (14), we obtain $I_{v,r}(k)$ in the form

$$I_{v,r}(k) = I^I_{v,r}(k) + I^S_{v,r}(k), \tag{67}$$

where the two terms correspond to the incident (I) and scattered (S) waves in Eqs. (14). The second term is given by

$$I^S_{v,r}(k) = (2\pi)^{1/2} \sum_{i,r,\sigma} \sigma e^{\mathrm{sgn}(S_r'')i\pi/4} \frac{|u_f(t_r)| W^\sigma_{v,i}(t_r)}{|(t_r - t_i)F(t_i)S_r''|^{1/2}} \exp\left[i\mathcal{S}(t_r;k) + i\mathcal{S}(t_r,t_i) + i\varepsilon_v t_r\right], \tag{68}$$

where

$$W^\sigma_{v,i}(t) = \sum_{v'} e^{-i\varepsilon_{v'}[t - t_i(t)]} S^{\sigma\,\mathrm{sgn}[u_f(t)]}_{vv'}[u_f(t)] g_{v'}[t_i(t)] \tag{69}$$

and

$$S_r'' = F(t_r)[u_f(t_r) - u_i(t_r,k)] + \frac{u_f^2(t_r)}{t_r - t_i}. \tag{70}$$

In these equations $t_r = t_r^\sigma(k)$, $t_i = t_i[t_r^\sigma(k)]$, and the summation in Eq. (68) runs over all triples (i,r,σ) identifying the different solutions to Eq. (66). The first term in Eq. (67) is given by the same Eq. (68), but with $S^{\sigma\,\mathrm{sgn}[u_f(t)]}_{vv'}[u_f(t)]$ in Eq. (69) replaced by $-\delta_{\sigma+}\delta_{vv'}$ and therefore $W^\sigma_{v,i}(t_r)$ replaced by $-\delta_{\sigma+}e^{-i\varepsilon_v(t_r - t_i)} g_v(t_i)$. Note that for a transmission in Eq. (66) ($\sigma = +$), the first term in Eq. (70) vanishes and the sum $\mathcal{S}(t_r;k) + \mathcal{S}(t_r,t_i)$ in the exponent in Eq. (68) coincides with the action $\mathcal{S}(t_i;k)$ in Eq. (65). Then it can be seen that

$$I^I_{v,r}(k) = -e^{i\pi/4}(2\pi)^{1/2} \sum_{L>0} L \sum_{i \in L\ \mathrm{loop}} \frac{g_v(t_i)}{|F(t_i)|^{1/2}} \times \exp[i\mathcal{S}(t_i;k) + i\varepsilon_v t_i], \tag{71}$$

where the two sums together run over the same set of transmission IRTs as in Eq. (65), but the set is now divided into subsets consisting of IRTs with the same number of loops L and the sum over i runs over the subset of L-loop IRTs. The factor L resulting from the sum over r in Eq. (68) accounts for L rescattering events (transmissions) which occur on an L-loop IRT, and because of this factor, the zero-loop IRTs do not contribute. For $\sigma = +$, the sum of the two terms in Eq. (67) with the same i and r introduces a correction to the term with the same i in Eq. (65) which accounts for electron-ion interaction in the transmission at time t_r. For $\sigma = -$, the first term in Eq. (67) does not contribute, while the second term accounts for contributions from IRTs with one reflection. The fact that these equations correctly account for only one rescattering event results from neglecting the electron-ion interaction in intermediate transmissions in contributions from multiloop CRTs in Eq. (62). Higher-order contributions from multiple rescatterings to the rescattering part of the ionization amplitude in the zero-range-potential model were analyzed in Ref. [83].

Equations (67), (68), and (71) give the leading-order term in the asymptotics of the rescattering part in Eq. (63) for $\epsilon_{nf} \to 0$. However, in the calculations below we resort to an additional approximation to simplify the implementation of these equations. If we would retain in Eq. (62) only contributions from one-loop CRTs, then Eq. (66) would describe only the first rescattering event on an IRT, the sum over i and r in Eq. (68) would contain only terms for which ionization and rescattering are connected by a one-loop CRT, and the factor L in Eq. (71) would disappear. In this approximation, $I^I_{v,r}(k)$ cancels all contributions to Eq. (65) from IRTs with $L > 0$, while the part of Eq. (68) with $\sigma = +$ restores these contributions, but with the first transmission treated correctly. Note that this approximation cannot be justified by smallness of ϵ_{nf}, because the neglected terms have the same order as the retained ones. We adopt it for practical reasons to simplify the calculations in Sec. VI.

C. Uniform asymptotics near a backward rescattering caustic

In Ref. [47] it was inferred on physical grounds from the results obtained by solving the TDSE for one-electron atoms that strong-field PEMDs in the region dominated by backward rescattered photoelectrons factorize into a product of the differential cross section for elastic scattering of an electron on the atomic potential and a returning photoelectron wave packet. In Ref. [65] the factorization formula was derived within the adiabatic theory [8] and it was shown that it holds in the vicinity of a backward rescattering caustic (BRC). In this section we generalize the results of Ref. [65] to the present model on the basis of the AAnf with the internuclear motion included in the consideration.

Consider IRTs with one reflection associated with the solutions to Eq. (66) for $\sigma = -$. In the general case, there can exist several such IRTs contributing to Eq. (68) at a given photoelectron momentum k. As k varies, the IRTs also vary continuously and may coalesce pairwise. The points on the k axis where such coalescences happen are BRCs in the present one-dimensional model. Let us introduce a function which is inverse to $t_r^-(k)$ defined by Eq. (66),

$$k(t_r^-) = v_\infty - 2v(t_r^-) + v(t_i(t_r^-)). \tag{72}$$

This equation gives the asymptotic momentum for an IRT with one reflection as a function of the reflection time. The BRCs can be found as local extrema of this function. Thus, the reflection time for a pair of coalesced IRTs at a BRC is defined by

$$\frac{dk(t_r)}{dt_r} = 2F(t_r) + \frac{u_f(t_r)}{t_r - t_i(t_r)} = 0 \to t_r = t_{rc}. \tag{73}$$

The ionization time for these IRTs is $t_i = t_i(t_{rc})$, the incident velocity before the reflection is $u_f = u_f(t_{rc})$, and the asymptotic momentum giving the position of the BRC is $k_c = k(t_{rc})$.

To simplify equations, in the rest of this section we use the shorthand notation t_r, t_i, and u_f for quantities characterizing the pair of coalesced IRTs at a particular BRC k_c. If k is close to k_c, the integrand in Eq. (40) defining the rescattering part in Eq. (63) has two closely located SPs associated with the coalescing IRTs. These SPs cannot be treated separately, which can be seen from the fact that the corresponding S_r''' defined by Eq. (70) turns to zero as $|k-k_c|^{1/2}$, and hence their contributions to Eq. (68) diverge as $|k-k_c|^{-1/4}$ at the BRC. By treating these SPs as a complex, we obtain the uniform asymptotics of the integral which holds at sufficiently small $|k-k_c|$. The derivation follows that in Ref. [65]; the result is

$$I_{v,c}(k) = \mathrm{Ai}(\alpha(k-k_q))\frac{2\pi\alpha W_{v,i}^{-}(\tilde{t}_r)}{|(t_r-t_i)F(t_i)|^{1/2}} \times \exp[i\mathcal{S}(\tilde{t}_r;k) + i\mathcal{S}(\tilde{t}_r,\tilde{t}_i) + i\varepsilon_v\tilde{t}_r]. \quad (74)$$

Here $\mathrm{Ai}(z)$ is the Airy function [85], its argument is defined by

$$\alpha = -\mathrm{sgn}(S_r''')u_f\left(\frac{2}{|S_r'''|}\right)^{1/3}, \quad (75)$$

and

$$k_q = k_c - q, \quad (76a)$$

$$q = \frac{\varepsilon_0 - E_0^{\mathrm{BO}}}{(t_r-t_i)F(t_i)}, \quad (76b)$$

and the time arguments marked with a tilde are

$$\tilde{t}_r = t_r + \frac{F(t_r)(k-k_c)}{S_r'''} \quad (77)$$

and $\tilde{t}_i = t_i(\tilde{t}_r)$, where

$$S_r''' = u_f\left[2\dot{F}(t_r) + \frac{3F(t_r)}{t_r-t_i} - \frac{4F^2(t_r)}{(t_r-t_i)F(t_i)}\right]. \quad (78)$$

The point k_q, where the argument of the Airy function in Eq. (74) turns to zero, is the quantum caustic [65]. It is shifted with respect to the corresponding classical caustic k_c. The quantum shift q is obtained by taking into account that $\varepsilon_v - \varepsilon_0 = O(\epsilon_n^1)$ and $e^{iE_0^{\mathrm{BO}}t}g_v(t)$ is a slow function of t, which also explains why it does not depend on v. Its magnitude scales as $O(\epsilon_f^1)$, so the shift disappears in the adiabatic limit. We mention that the quantum shift of a BRC predicted in Refs. [65,86] was recently observed experimentally [64]. The uniform asymptotics given by Eq. (74) replaces the sum of individual contributions from the two coalescing IRTs in Eq. (68). It holds in an interval $|k-k_c| = o(\epsilon_f^{-1})$ [65], which includes both classical k_c and quantum k_q caustics.

The intervals of the k axis where the adiabatic and rescattering parts in Eq. (63) contribute to the PEMD (34) depend on the shape of the pulse $F(t)$. For monochromatic pulses, the high-energy parts of the PEMD at both positive and negative k are dominated by backward rescattered photoelectrons [45], and the same holds for typical few-cycle pulses. In this case, there exist outermost BRCs in each direction of the k axis. Near such a BRC k_c, there are no other contributions to Eq. (63) except for that from the two coalescing IRTs. The PEMD in this region is given by

$$P_{v,c}(k) = |I_{v,c}(k)|^2 = \mathrm{Ai}^2(\alpha(k-k_q))\frac{4\pi^2\alpha^2|W_{v,i}^{-}(\tilde{t}_r)|^2}{|(t_r-t_i)F(t_i)|}. \quad (79)$$

This is the analog of the factorization formula proposed in Ref. [47] and derived in Ref. [65] for the present model. The factor $|W_{v,i}^{-}(\tilde{t}_r)|^2$ incorporates information on both ionization and rescattering processes represented by the last factor and the scattering matrix in Eq. (69), respectively. These processes are entangled in Eq. (69), because of their multichannel character reflecting the existence of internal degrees of freedom in the molecular ion. This feature indicates an essential difference between molecular systems with the internuclear motion included and one-electron atoms or molecules with frozen nuclei considered in Refs. [47,65]. The main virtue of the factorization formula in the latter case is that it enables one to extract the differential cross section from experimentally observable PEMDs [48–64]. In this sense, the situation in the former case is much more complicated. Yet Eq. (79) also can be used for extracting some structure information from the PEMD, in the spirit of Refs. [47,65], as we show below.

D. Born-Oppenheimer approximation for rescattering

The asymptotics of the rescattering parts of the wave function in Eq. (46) and ionization amplitude in Eq. (63) obtained above are expressed in terms of the exact molecular scattering state and scattering matrix, respectively. In this section we rewrite these asymptotics using the BOA, which makes them simpler and suggests a transparent picture describing the dynamics of the nuclear subsystem.

We begin with the wave function. Equation (57) gives the amplitude of ionization from the state (47) into channel v. Using the completeness of the set of ionic eigenstates $\chi_v(R)$, we can change the representation from v to R and obtain the corresponding amplitude of ionization at point R,

$$g(R,t) = \sum_v g_v(t)\chi_v(R) = f(R,F(t))\Psi(R,t). \quad (80)$$

Then substituting Eq. (21) for the molecular scattering state into Eq. (62) gives

$$\Psi_r(x,R,t) = \sum_i \frac{w_i(R,t)}{|(t-t_i)F(t_i)|^{1/2}}\phi_e^{(+)}(x;R,u_f(t))e^{i\mathcal{S}(t,t_i)}, \quad (81)$$

where

$$w_i(R,t) = e^{-iH_{\mathrm{ion}}(t-t_i)}g(R,t_i). \quad (82)$$

The function $g(R,t_i)$ has the meaning of the nuclear wave packet in the molecular ion created as a result of ionization at time t_i. This wave packet is determined by the solution to the nuclear TDSE (48) and the ionization amplitude in the electronic SS defined by Eq. (25), both taken at the ionization time t_i. The function $w_i(R,t)$ is the result of the evolution of this wave packet driven by the Hamiltonian (9) until time t, while the electron travels along a CRT. The first factor in Eq. (81) gives the amplitude of the plane wave representing the electron arriving for rescattering at time t at a given internuclear distance R [instead of in a given channel v, as in

Eq. (62)], and the electronic scattering state is what the plane wave turns into after rescattering.

We now turn to simple (68) and uniform (74) asymptotics of the ionization amplitude. They contain the molecular scattering matrix through the function (69). Substituting Eq. (22) for the scattering matrix into this function and changing the representation, as in Eq. (80), we present it in the form

$$W^{\sigma}_{v,i}(t) = \int_0^{\infty} \chi_v(R) W^{\sigma}_i(R,t) dR, \tag{83}$$

where

$$W^{\sigma}_i(R,t) = \sum_v W^{\sigma}_{v,i}(t)\chi_v(R) = S^{\sigma\,\mathrm{sgn}[u_f(t)]}(u_f(t);R) w_i(R,t). \tag{84}$$

Thus Eqs. (68) and (74) can be expressed in terms of $W^{\sigma}_i(R,t)$. This function has the meaning of the nuclear wave packet in the molecular ion after the rescattering at time t has occurred. It factorizes into a product of the electronic scattering matrix and the nuclear wave packet before rescattering $w_i(R,t)$. Thus, as a result of rescattering, the nuclear wave packet is multiplied by the electronic scattering matrix. We will see below that it is the wave packet (84) after rescattering which can be reconstructed from the PEMD using Eq. (79).

Substituting Eq. (83) into Eq. (79), we obtain the total PEMD near a BRC,

$$P_c(k) = \sum_v P_{v,c}(k) = \mathrm{Ai}^2(\alpha(k-k_q)) \frac{4\pi^2\alpha^2 N}{|(t_r - t_i)F(t_i)|}, \tag{85}$$

where

$$N = \sum_v |W^{-}_{v,i}(\tilde{t}_r)|^2 = \int_0^{\infty} |W^{-}_i(R,\tilde{t}_r)|^2 dR \tag{86}$$

is the norm of the nuclear wave packet (84) after reflection of the electron.

V. ILLUSTRATIVE CALCULATIONS

In this section we show the quantitative performance of the adiabatic theory through illustrative calculations. We validate the theory by comparing PEMDs obtained using the AAnf with accurate direct reference solutions of the TDSE and show the convergence of the AAnf results to the TDSE results in the adiabatic limit. We then explore specific features of the PEMDs, before showing how target information such as the scattering matrix or the ionic nuclear wave packet can be reconstructed from the TDSE results.

We consider one-cycle pulses with the Gaussian envelope of the form

$$F(t) = -F_0\sqrt{2e}\tau \exp(-\tau^2), \quad \tau = \frac{2t}{T}, \tag{87}$$

where F_0 is the maximal field strength and T is the pulse duration. This pulse has only one zero at $t = 0$ and rescattering can only occur after the field passes through this zero, and thus it is most suitable for testing the theory [83]. We now discuss the kinematics of the IRTs associated with the one-cycle pulse [Eq. (87)]. In Figs. 5(a) and 5(b) we show ionization times t_i as a function of asymptotic momentum k for several of the simplest IRTs together with the shape of the pulse. In Fig. 5(c) we also plot the momentum that an electron has right before

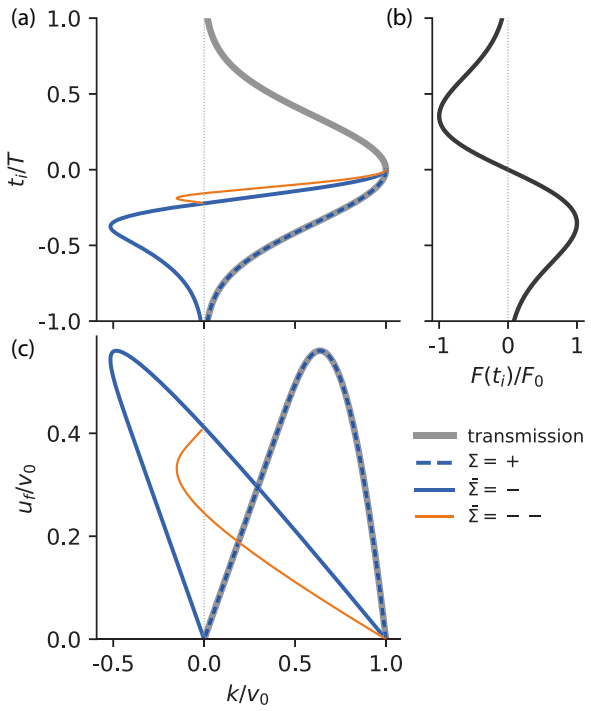

FIG. 5. Time of ionization t_i and velocity before rescattering u_f of IRTs for the one-cycle pulse (87). (b) shows the shape of the pulse. On the horizontal axis in (a) and (c) is the final momentum of the electron at the end of the pulse k, scaled by v_0. The vertical axis in (a) and (b) shows the time of ionization t_i. Shown on the vertical axis in (c) is $u_f(t_1, t_i)$, the incoming velocity at the first rescattering event. The thick solid gray lines show transmission IRTs that contribute to $I_{v,a}(k)$ [Eq. (65)]. These have an empty reduced signature $\bar{\Sigma}$. For $t_i > 0$ these have an empty signature Σ, while for $t_i < 0$ they have $\Sigma = +$. Medium thick blue lines show all one-loop IRTs and a two-loop IRT that contribute to $I_{v,r}(k)$ at the leading order. The dashed blue lines show $\Sigma = +$, which is also shown by part of the gray line. The solid blue lines show $\bar{\Sigma} = -$. For $k < 0$ they have $\Sigma = -$ and for $k > 0$ they have $\Sigma = -+$. Thin solid orange lines show IRTs with $\bar{\Sigma} = --$. Note that this figure is the same for any value of F_0 and T.

scattering u_f, for the same IRTs as in Figs. 5(a) and 5(b), except for the zero-loop transmission IRT for which u_f is not defined. In the figure k is scaled by its maximal value of $v_0 = \frac{\sqrt{2e}}{4} F_0 T$ for the present pulse shape (see Ref. [83]). The gray lines designated as transmission are for a zero-loop IRT with empty Σ for $t_i > 0$ and a one-loop IRT with $\Sigma = +$ for $t_i < 0$. They are obtained by the solutions to Eq. (64) and contribute to the adiabatic part of the ionization amplitude, $I_{v,a}(k)$ in Eq. (65). The dashed blue lines indicated by $\Sigma = +$ are for a one-loop IRT, given by the solutions to Eq. (66) with $\sigma = +$, contributing to the rescattering part, $I_{v,r}(k)$ in Eq. (67). The solid blue lines designated as $\bar{\Sigma} = -$ are for one-loop IRTs with $\Sigma = -$ in the interval $-0.516 < k/v_0 < 0$ and a two-loop IRT with $\Sigma = -+$ for $0 < k/v_0 < 1$. They are obtained from the same equation as the dashed blue line, but with $\sigma = -$, and also contribute to $I_{v,r}(k)$. For $\Sigma = -+$ we only consider the interaction in the first rescattering event. These are the IRTs that contribute to the leading-order terms

of $I_{v,a}(k)$ and $I_{v,r}(k)$ and are taken into account in our AAnf calculations.

We note that it is not possible to have any additional rescattering events after a transmission for the pulse,[1] so all IRTs that contribute to the leading-order terms of $I_{v,a}(k)$ and $I_{v,r}(k)$ in the asymptotics of the ionization amplitude (63) are considered in our calculations without the approximation mentioned at the end of Sec. IV B. As also mentioned at the end of Sec. IV B, $I^I_{v,r}(k)$ from the one-loop transmission IRT with $\Sigma = +$ cancels $I_{v,a}(k)$ from the same IRT at each SP, leaving only the $I^S_{v,r}(k)$ term in Eq. (67). This is indicated by the overlap of the dashed blue line and part of the gray line in Fig. 5. In addition to the zero and one-loop IRTs mentioned above, there exist multiloop IRTs that contribute to higher-order terms. Although they are not included in the calculations, the orange line in Fig. 5 shows an example of a two-loop IRT with $\bar{\Sigma} = --$ in the interval of $-0.151 < k/v_0 < 1$ to be discussed in the following sections.

For the calculations in this section we use the hydrogenic nuclear mass of $M = 1836$ except where otherwise stated. We use the same numerical methods for solving the TDSE and finding the exact molecular scattering states as in Ref. [44] (see the Appendix therein for details).

A. General structure of vibrationally resolved photoelectron momentum distributions

In Figs. 6 and 7 we compare the partial PEMDs $P_v(k)$ for $v = 0, 1, 2$ from the TDSE [Eq. (34)] and simple AAnf [using Eq. (63) with Eqs. (65) and (67), with the exact scattering matrix]. The critical field that indicates the boundary between tunneling and over-the-barrier regimes of ionization in the present case is estimated as $F_c = 0.156$, using the criterion in Ref. [44]. The $F_0 = 0.1$ for Fig. 6 and $F_0 = 0.2$ for Fig. 7 belong to the tunneling and over-the-barrier regimes, respectively. As in Refs. [44,70], the critical field below which the BOA breaks down when describing tunneling ionization is $F_{\mathrm{BO}} \approx 0.05$. The BOA thus holds for describing ionization at the field values considered. We present the partial PEMDs for $T = 50$ and 150 at each F_0 in Figs. 6 and 7. The timescale of the field T_f is estimated to be $T/2$ for the one-cycle pulse. The $T_f = 25$ for the shorter pulses is slightly longer than the electronic timescale of $T_e = 11$, corresponding to near the onset of the adiabatic regime [44], while $T_f = 75$ for the longer pulses is beyond the onset. The computational requirements of solving the TDSE limits the largest T we can consider, but the present values are sufficient for testing the theory. There are no such computational limitations in AAnf calculations.

The main goal of this section is to demonstrate the convergence of the AAnf to the TDSE in the adiabatic limit

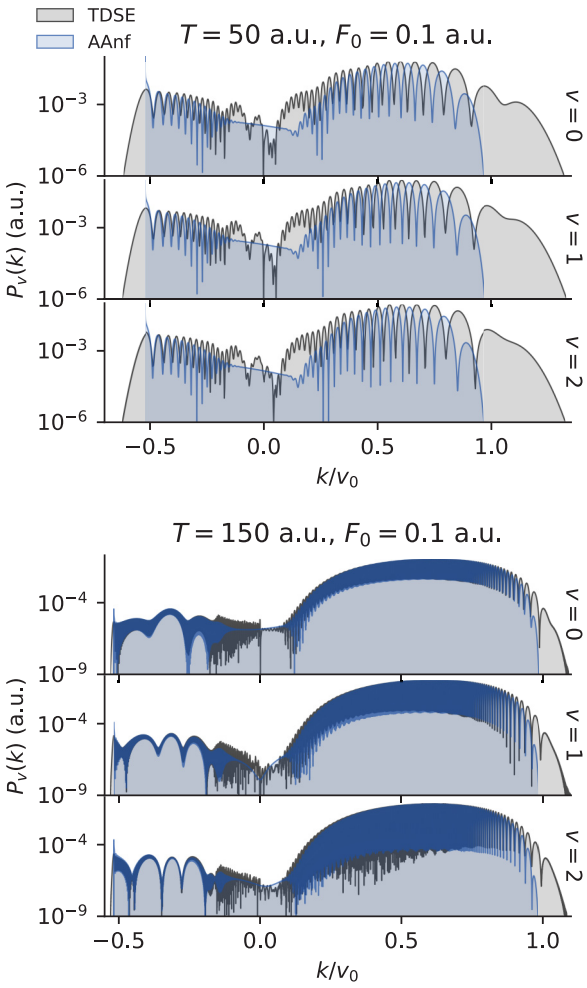

FIG. 6. Partial PEMDs $P_v(k)$, generated by one-cycle pulses for a tunneling field strength $F_0 = 0.1$ with durations T indicated in the figure. The TDSE results (black lines) are obtained using Eq. (34) and simple AAnf results (blue lines) using Eq. (63) with Eqs. (65) and (67) (using exact scattering matrix). The final electron momentum k has been scaled by v_0.

$\epsilon_{nf} \to 0$. The agreement between the TDSE and AAnf results for the partial PEMDs is seen to generally be quite good for both tunneling and over-the-barrier regimes, and the agreement improves as T is increased for fixed F_0, showing the convergence of the AAnf in the large-T limit. It is also seen that better agreement is achieved for the stronger pulses, when comparing to the same value of T. We expect that the agreement is further improved for longer pulses. However, there still remain regions with slow convergence for k near zero and on the left and right edges of the PEMDs. For $0 < k/v_0 < 1$ contributions from transmission IRTs dominate since reflection elements of the scattering matrix are small for the relevant values of u_f, except near $k = 0$, where the contributions from transmission IRTs drop to zero.[2]

[1]The one-cycle pulse (87) is antisymmetric and has $F(t) > 0$ for $t < 0$ and $F(t) < 0$ for $t > 0$. Since the pulse's only sign change is at $t = 0$, rescattering events can only happen at $t > 0$ with ionization times at $t_i < 0$. Before the first rescattering event, all trajectories will have $u_f(t_1, t_i) > 0$. If the electron is transmitted, its velocity just after rescattering and the field-induced acceleration will both be positive. A transmitted electron will thus only be able to move in the positive direction and will therefore never return to the origin.

[2]This can be explained by looking at Fig. 5. There it can be seen that $k \to 0$ corresponds to $|t_i| \to \infty$ for the transmission IRTs (gray lines). In the $|t_i| \to \infty$ limits, the field goes to zero and the $g_v(t_i)$ coefficients become exponentially small.

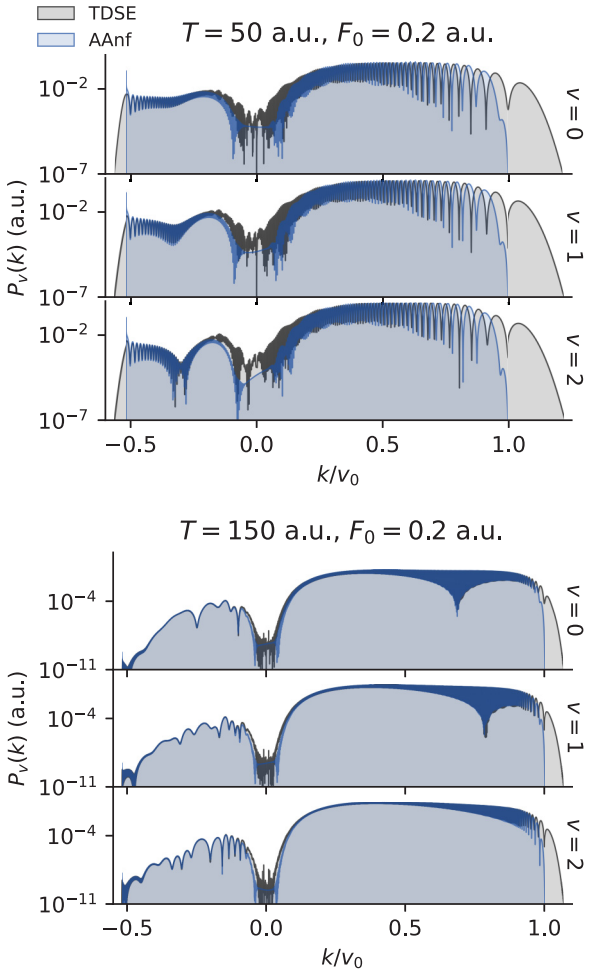

FIG. 7. Same as Fig. 6 for $F_0 = 0.2$ in the over-the-barrier regime.

Higher-order terms from multiloop IRTs, such as the $\bar{\Sigma} = --$ IRT indicated by the orange lines in Fig. 5, only contribute for the interval of $-0.151 < k/v_0 < 1$. The discrepancy between the TDSE and AAnf results in the interval $-0.151 < k/v_0 \lesssim 0.1$ is caused by those higher-order terms. At the left cutoff near $k/v_0 = -0.516$ where the reflection IRTs has a caustic, the simple AAnf diverges, while the TDSE drops off gradually. This can be remedied using the uniform AAnf, and in Sec. V C we take a closer look at this using the uniform expansion around the caustic developed in Sec. IV C. Near the right cutoff where $k/v_0 \sim 1$ we see that the AAnf results fall off faster than the TDSE results.[3] The same feature was seen in Ref. [44]. This disagreement can be remedied by using the uniform adiabatic theory as in Ref. [8], but this is beyond the scope of the present work. We note that even though convergence is slow near $k = 0$ and the edges of the PEMD, the AAnf results with the leading-order terms will eventually converge to the TDSE results for sufficiently large T.

[3]The AAnf PEMDs going to zero as $k/v_0 \to 1$ can be understood by inspecting Fig. 5. There it can be seen that for $k/v_0 \to 1$, t_i approaches 0 for all IRTs. The field $F(t_i)$ has a zero there, which causes $g(t_i)$ and thereby the PEMD to also go to zero.

Let us next discuss the oscillatory structures that appear in the PEMDs. The structures can be explained by an interference between contributions to $I_v(k)$ from different IRTs for each k (see Fig. 5). For $0 < k/v_0 < 1$, there are three IRTs contributing to the leading-order terms of $I_{v,a}(k)$ and $I_{v,r}(k)$. Considering the cancellation among the contributions discussed above, three ionization amplitude terms are left, namely, $I_{v,a}(k)$ from the zero-loop transmission IRT, $I^S_{v,r}(k)$ from the one-loop IRT with $\Sigma = +$, and $I^S_{v,r}(k)$ from the two-loop IRT with $\Sigma = -+$. Let us call them I_a, I_+ and I_-, respectively, for brevity. For $k/v_0 \gtrsim 0.1$, the PEMDs are dominated by the contributions from the two terms I_a and I_+. The contrast of the oscillation is determined by the relative amplitudes of the two terms at each k. In some places the contrast is seen to vary significantly with k. For instance, for $F_0 = 0.2$, $T = 150$, and $v = 0$ in Fig. 7, a high contrast can be observed at $k/v_0 = 0.7$, where the amplitudes of the two terms are interchanged. The AAnf result perfectly reproduces this feature. Near $k = 0$, the contributions from I_a and I_+ drops to zero and become comparable to that from I_- at $k/v_0 \sim 0.1$. This causes a modulation of the oscillation, but such a structure is hardly seen on the scale of Figs. 6 and 7. We will discuss this in more detail in the next section.

In the range of $-0.516 < k/v_0 < -0.151$, $P_v(k)$ has contributions from only two terms associated with the $\Sigma = -$ IRTs. This one-cycle pulse is thus suitable for testing the adiabatic theory, since we can cleanly assign one-loop reflection IRTs to observations in this momentum range. We can observe a complicated nonuniform interference structure that strongly depends on v in this region. The structure can be explained by the AAnf as follows. In the AAnf, the PEMDs are obtained from summations of the leading-order terms over all SPs and intermediate channels v'. The structures seen in the PEMD depend on all of these terms and on the detailed phases of each term. In the fixed nuclear case, similar structures appear, and in that case those structures exactly reflect the structure of the scattering matrix which is related to two-center interference. The interference structures here are also related to the structure of the scattering matrix, but due to the summation over v' there is no easy way to relate these structures to specific scattering matrix contributions. As can be seen in Fig. 2, for reflected electrons at moderate negative values of k, the scattering matrix has comparable magnitudes across different v. For the heavy nuclear masses considered here, the $g_{v'}(t)$ coefficients will change slowly with v', meaning that they will also have comparable magnitudes across neighborhoods of v'. This means that many channels will contribute at an equal level in Eq. (69). It is thus essential to include all these channels in order to reproduce the structures seen in this region. We wish to emphasize that the present theory reproduces the TDSE results really well, while the fixed nuclei approximation is completely unable to explain these structures.

For $-0.516 < k/v_0 < -0.151$, the contrast of the fast oscillation in the PEMDs in Figs. 6 and 7 for a number of pulse parameters is seen to be very small, to the extent that the oscillation cannot be seen. This is, for instance, very clear for $F = 0.1$, $T = 150$, and $v = 2$ in Fig. 6 or at any v for $F = 0.2$ and $T = 150$ in Fig. 7. We can explain this by considering u_f in Fig. 5(c). There we see that the values of u_f for the two $\Sigma = -$ IRTs at the same value of k for $k < 0$ are quite

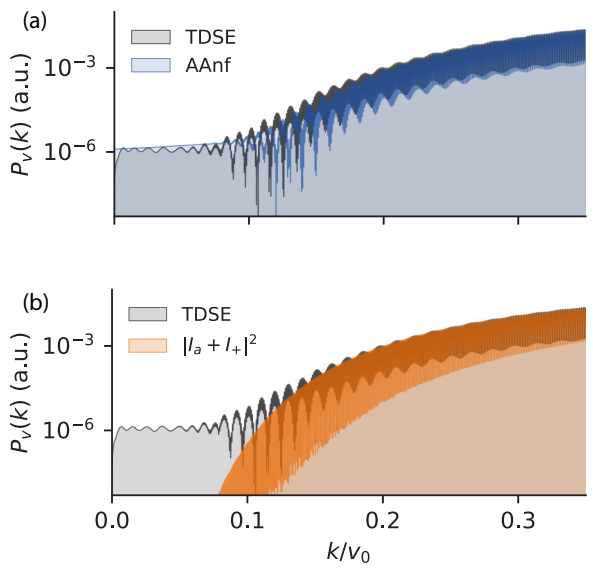

FIG. 8. (a) Close-up of the TDSE and AAnf partial PEMDs in Fig. 6 for $v = 0$, $T = 150$, and $F_0 = 0.1$. (b) The AAnf result has been replaced by the orange line showing $|I_a + I_+|^2$, which is the AAnf result with the reflection contribution left out.

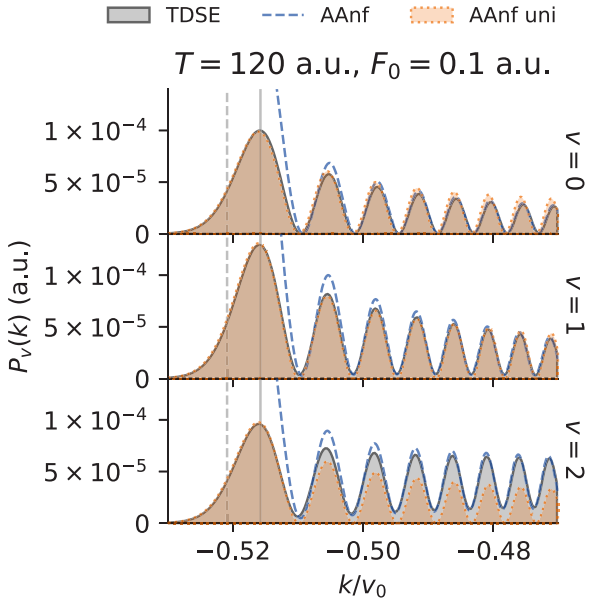

FIG. 9. Partial PEMDs near the BRC on a linear scale. The TDSE and AAnf results are calculated the same way as in Fig. 6. The uniform AAnf results shown by the orange area with a dashed edge are calculated using Eq. (74). The vertical solid gray line on the right shows the classical caustic k_c. The vertical dashed gray line on the left shows the quantum caustic k_q.

different. From Fig. 2 we also see that the reflection part of the scattering matrix decays exponentially in $|u_f|$. This indicates that the contribution from the IRT with the smaller value of u_f will be much larger than the contribution from the other IRT, and the contrast between these two contributions is thus very small. This becomes more pronounced in the adiabatic limit since $|u_f| \propto TF_0$.

Summarizing, we see that the AAnf results including IRTs that contribute up to the leading order in $I_{v,a}(k)$ and $I_{v,r}(k)$ reproduce TDSE results well in the adiabatic regime and the agreement improves as T is increased.

B. Rescattering-induced modulation at $k > 0$

As mentioned in the preceding section, the three terms from zero-, one-, and two-loop IRTs are almost comparable at $k/v_0 \sim 0.1$ and this induces modulation in the oscillation of $P_v(k)$. This modulation is clearly visible in the expanded view of the PEMD in Fig. 8 for $F_0 = 0.1$ with $T = 150$ and $v = 0$. For $k/v_0 \gtrsim 0.1$, on top of a very rapid oscillation, there is a slower modulating oscillation, which is most prominent around $k/v_0 = 0.2$ and becomes weaker as k increases. This modulation structure is similar in amplitude and frequency in the TDSE and AAnf results, but is shifted in phase between the two, likely due to contributions from higher-order terms from multiloop IRTs. Still, the overall modulation structure appears to be similar between the TDSE and AAnf, so we proceed to analyze it within the AAnf with the leading-order terms.

Using the same I_a, I_+, and I_- symbols for the three terms as in the preceding section, the PEMD at each k can be expressed as

$$\begin{aligned} |I_a + I_+ + I_-|^2 = {} & |I_a|^2 + |I_+^2 + |I_-|^2 + 2|I_a I_+| \cos(\phi_a - \phi_+) \\ & + 2|I_a I_-| \cos(\phi_- - \phi_a) \\ & + 2|I_- I_+| \cos(\phi_- - \phi_+), \end{aligned} \tag{88}$$

where $\phi_i = \arg I_i$. For most values of k, except near $k = 0$, $|I_a|$ and $|I_+|$ are of similar magnitude, while $|I_-|$ is smaller than the other two. This can be inferred from the information in Fig. 5. Here we see that for k near 0, u_f for the $\Sigma = -+$ IRT is quite large. From Fig. 2 we know that the scattering matrix is small for reflection with large u_f, which makes the contribution to the ionization amplitude (68) here small. As k approaches v_0, Fig. 5 shows that u_f approaches zero, but so does t_i. At $t_i = 0$ the field is zero, meaning that the $g_v(t_i)$ coefficients are small around here. So in either case the contribution to the ionization amplitude from the $\Sigma = -+$ IRT is small due to either smallness of the scattering matrix or smallness of $g_v(t_i)$. In the case where $|I_-| = 0$, there is only one cosine term in Eq. (88) and thus no modulation of the PEMD. We illustrate this in Fig. 8, where the orange line in Fig. 8(b) shows $|I_a + I_+|^2$, which is the result of only including the I_a and I_+ contributions, i.e., leaving out the reflection IRT I_- contribution. We indeed see that only the fast oscillation remains and the slow modulation has disappeared. The modulation is thus seen to be a signature of the reflection contribution. By comparing Figs. 8(a) and 8(b) we also see how the reflection contribution dominates near $k = 0$, when the transmission IRT contributions have died out.

C. Backward rescattering caustic

Here we illustrate the uniform AAnf near a BRC developed in Sec. IV C. In Fig. 5 it can be seen that the reflection $\Sigma = -$ IRTs have a BRC at $k/v_0 = -0.516$. Figure 9 shows a close-up of partial PEMDs near this BRC for field parameters $F_0 = 0.1$ and $T = 120$, which is in the adiabatic regime. In Sec. IV C it was shown that the simple AAnf result diverges

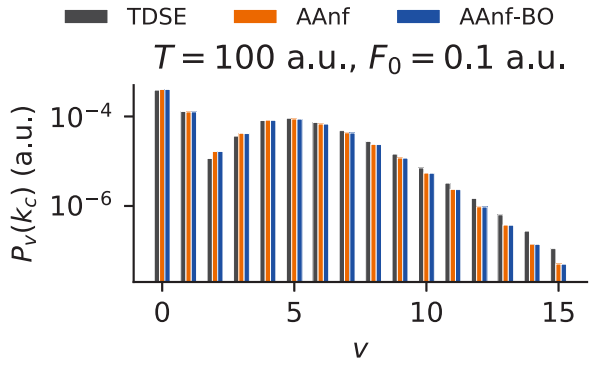

FIG. 10. The PEMD $P_v(k_c)$ evaluated at the classical caustic k_c for $M = 1836$. The AAnf results are for the uniform AAnf (74). The AAnf BO result additionally uses the BOA for the scattering matrix (83).

at the BRC as $|k - k_c|^{-1/4}$, and in the figure we clearly see this divergence. For $k/v_0 < -0.516$ the simple AAnf result is not defined, while for $k/v_0 > -0.516$ simple AAnf results are seen to agree well the TDSE results, except at the BRC. On the other hand, the uniform AAnf results are defined on both sides of the BRC and they are seen to agree quite well with the TDSE results on both sides of and at the BRC. We note that the uniform AAnf is based on an expansion in k around k_c, so it only works well in a neighborhood around k_c. We also perform calculations for the uniform AAnf using the BOA for the scattering matrix as described in Sec. IV D. On the scale of the figure these results are indistinguishable from the full uniform AAnf results, so we only include the latter in the figure. Figure 9 also illustrates the quantum caustic k_q. The argument of the Airy function in the uniform AAnf (74) is zero at $k = k_q$. Around this point the Airy function changes from being exponential to being oscillatory in nature, as can also be seen in the figure.

In the next two sections we will use $P_v(k_c)$, i.e., the PEMD evaluated at the classical caustic k_c, to reconstruct the scattering matrix and the ionic nuclear wave packet. A necessary prerequisite for this reconstruction is good agreement between the TDSE and AAnf for this quantity. We therefore examine the v dependence of $P_v(k_c)$ in Fig. 10 for $F = 0.1$ and $T = 100$, which is in the adiabatic regime. Since the AAnf result diverges at k_c, we are here only considering the uniform AAnf. In the figure we see that $P_v(k_c)$ has a small local minimum around $v = 2$, but otherwise decays monotonically as v increases. The figure shows that the uniform AAnf (74) reproduces the TDSE results quite well. It can also be seen that using the BOA for the scattering matrix in the AAnf (83) agrees very well with the results using the exact scattering matrix. This is expected since we see good agreement between the exact and BO scattering matrices in Fig. 2.

D. Reconstructing scattering matrix

Suppose we did an experiment and measured $P_{v,c}(k_c)$. Would it be possible to reconstruct the electronic scattering matrix or the ionic nuclear wave packet? Equation (74) suggests an affirmative answer to this question, and we outline the extraction procedure below. We do not have experimental results available for this work, so in the following we use the TDSE results as a substitute. In Eq. (74) the only dependence on v enters through $W^-_{v,i}(\tilde{t}_{rc})$. For $k = k_c$ we have $\tilde{t}_{rc} = t_{rc}$. For fixed k, expressing the factors other than $W^-_{v,i}(t_{rc})$ on the right-hand side of Eq. (74) as a constant A, we can reconstruct $W^-_{v,i}(t_{rc})$ as

$$W^-_{v,i}(t_{rc}) = \frac{1}{A} e^{i\arg[I_{v,c}(k_c)]} \sqrt{P_{v,c}(k_c)}, \tag{89}$$

where $A = \mathrm{Ai}(-\alpha q) \frac{2\pi\alpha}{|(t_{rc}-t_i)F(t_i)|^{1/2}}$ is independent of v and $t_i = t_i(t_{rc})$. Here we omitted some constant action phase factors that are not essential for the reconstruction. In Eq. (89) we split the ionization amplitude $I_{v,c}(k_c)$ into its magnitude $[\sqrt{P_{v,c}(k_c)}]$ and phase $(\arg[I_{v,c}(k_c)])$ parts. Since in an experiment we would only be able to measure the phaseless quantity $P_{v,c}(k_c)$, we use phases from the AAnf, but magnitudes from experiment, here replaced by the TDSE. The $\chi_v(R)$ functions form a complete basis set, so by using Eq. (84) we can reconstruct the nuclear wave packet just after rescattering $W^-_i(R, t_{rc})$. When we assume that either the nuclear wave packet or the electronic scattering matrix is known, the other can be reconstructed. In the rest of this section we present the reconstruction procedure of the scattering matrix, assuming the nuclear wave packet is known. In the next section we discuss the other case.

Assuming that the AAnf wave packet $w_i(R, t_{rc})$ is known, we can then reconstruct the scattering matrix by dividing through with the wave packet in Eq. (84) to get

$$S^{-\mathrm{sgn}[u_f(t_{rc})]}(u_f(t_{rc}); R) = \frac{W^-_i(R, t_{rc})}{w_i(R, t_{rc})}. \tag{90}$$

Such a reconstruction is shown in Fig. 11(a). We see that the reconstruction works quite well for R between 1.5 and 3.2, but outside this range the reconstructed wave packet diverges. This problem is caused by the nuclear wave packet being localized in a small range of R, so for R outside this range, the nuclear wave packet is very small, which leads to the poor quality of this reconstruction. We can thus only get a reliable scattering matrix reconstruction in a small patch of R values with this method.

This can be partly remedied by combining reconstruction procedures for different values of T, where the nuclear wave packet due to its motion is localized around different R. When we keep the product TF_0 constant in these calculations, k_c and $u_f(t_{rc})$, which are related by $k_c/u_f(t_{rc}) = -1.05$, do not change and we can reconstruct the same scattering matrix at different values of R. The mapping between k and $u_f(t_r)$ can be seen in Fig. 5(c). Combining different sets of such results allows us to reconstruct the scattering matrix in the region of R where the nuclear wave packet has some weight at some time during its motion. Additional patches of reconstructed scattering matrix are illustrated in Fig. 11(b). In Fig. 11(a) vertical dashed lines show the boundaries of the classically allowed region for the nuclear motion. We expect to obtain a decent reconstruction result inside these boundaries. The reconstruction may extend a bit beyond this region due to the extent of the wave packet, but not by much.

To reconstruct the scattering matrix outside this range we need to make some additional assumptions. As can be seen

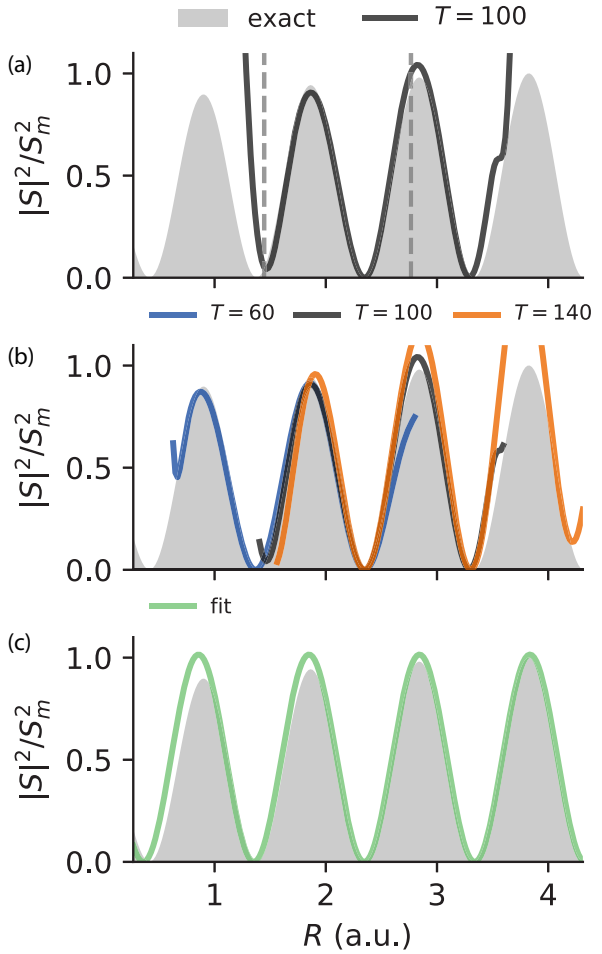

FIG. 11. Reconstruction of the electronic scattering matrix from TDSE results at the $u_f(t_{rc})$ that corresponds to k_c for $M = 1836$. Gray areas in all panels show the known exact electronic scattering matrix. Black lines in (a) and (b) show the result after dividing the reconstructed nuclear wave packet after scattering $W_i^-(R, t_{rc})$ with the known AAnf nuclear wave packet $w_i(R, t_{rc})$ [Eq. (90)] for $T = 100$. Blue and orange lines in (b) show the same for $T = 60$ and 140, respectively. The green line in (c) shows a fit to the reconstructed nuclear wave packet just after rescattering at $T = 100$ using Eq. (91). The product $TF_0 = 10$ is fixed throughout the figure, corresponding to $k_c = -3.32$ and $u_f(t_{rc}) = 3.16$. Vertical dashed lines in (a) show the classical turning points for the nuclear wave packet R_t defined by $U_{\text{ion}}(R_t) = \langle w_i|H_{\text{ion}}|w_i\rangle_R/\langle w_i|w_i\rangle_R$, found using the AAnf nuclear wave packet.

in Fig. 11, it appears that the scattering matrix would be well described by a sinusoidal function in R. This can be explained as resulting from two-center interference, which suggests the sinusoidal function should have wave number $u_f(t_{rc})$ in its argument. We then fit the absolute value of an expression of the following form to the absolute value[4] of the reconstructed nuclear wave packet just after rescattering at the caustic $|W_i^-(R, t_{rc})|$:

$$W_i^-(R, t_{rc}) = S_0 \cos[-u_f(t_{rc})R + \delta] w_i(R, t_{rc}). \tag{91}$$

[4]For simplicity of the analysis, we ignore phases and look only at the shape in this fitting reconstruction.

Here the known numerical values of $w_i(R, t_{rc})$ are used in the fitting procedure and S_0 and δ are parameters to be fit. The reconstructed scattering matrix is then given by $S_0 \cos[-u_f(t_{rc})R + \delta]$, which can be calculated after the fitting is done. In Fig. 11(c) the results of this fitting procedure can be seen. Good agreement is seen across a large range of R, except for $R \lesssim 1$, where the assumption of a sinusoidal scattering matrix breaks down, due to the two atomic potential centers overlapping and eventually merging into one. Note that we are here using a finite range electron-nuclear interaction potential, where the overlap between the wells quickly disappears as R grows. For a potential with a Coulomb tail this would happen more slowly as R increases, and the scattering matrix would therefore perhaps depart more from the sinusoidal form than it is seen here for the finite range potential.

It is also possible to reconstruct the scattering matrix at different values of $u_f(t_{rc})$ by varying the product TF_0, since the former is proportional to the latter. Such a reconstruction result is shown in Fig. 12. By comparing this to the known exact electronic scattering matrix in Fig. 3 we see that the reconstruction works fairly well.

Finally, by using Eq. (22) we can reconstruct the exact two-dimensional scattering matrix from the reconstructed electronic scattering matrix. In Fig. 13 we compare such a reconstruction based on fitting with the known exact scattering matrix, which is also shown in Fig. 2. We see that for the range of k where we could do the reconstruction, the agreement is quite good.

E. Reconstructing the moving nuclear wave packet

In this section we present the reconstruction procedure for the nuclear wave packet, assuming the electronic scattering matrix to be known. As in the preceding section we take PEMD amplitudes from the TDSE results and phases from the AAnf results to reconstruct the nuclear wave packet just after rescattering $W_i^-(R, t_{rc})$ from Eq. (84). From this we could divide by the known electronic scattering matrix to obtain the nuclear wave packet. However, due to numerical imperfections in our reconstruction, the zeros of our reconstructed $W_i^-(R, t_{rc})$ would not exactly coincide with the zeros of the scattering matrix. This means that such a division would result in divergences appearing near zeros of the scattering matrix. Instead, we use a fitting procedure similar to Eq. (92), using the known scattering matrix. The nuclear wave packet is described by a Gaussian form of

$$W_i^-(R, t_{rc}) = S^{-\text{sgn}[u_f(t_{rc})]}(u_f(t_{rc}); R) A \exp\left[-\left(\frac{R - R_0}{\Delta R}\right)^2\right], \tag{92}$$

where A, R_0, and ΔR are parameters to be fit. After fitting, the wave packet can then be calculated as $A \exp[-(\frac{R-R_0}{\Delta R})^2]$. In the following calculations for reconstructing the nuclear wave packet in Figs. 14 and 15, we keep F_0 fixed while varying T, unlike above where we kept the product TF_0 fixed.

We explore the nuclear mass M dependence of the nuclear wave packets in Fig. 14. Here we use a tunneling field strength of $F_0 = 0.1$ for which the nuclear wave function $\Psi(R, t)$ does not decay much. For instance, for $M = 1836$ we have 5.5%

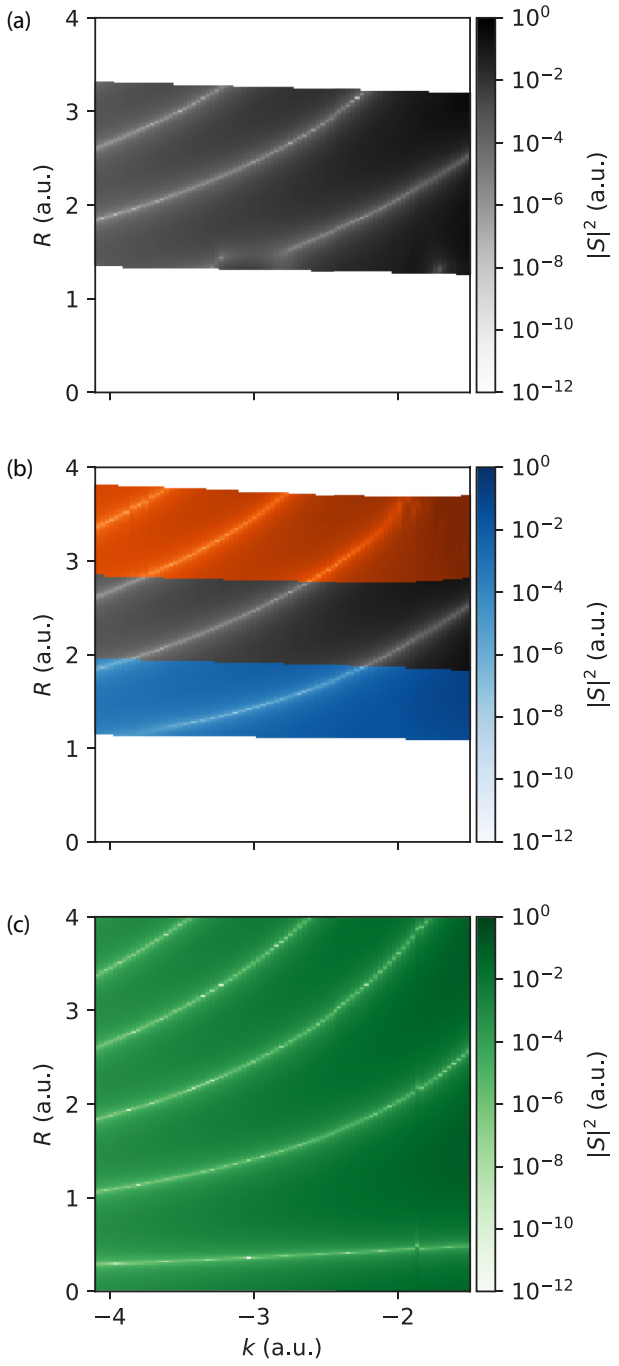

FIG. 12. Reconstruction of electronic scattering matrix from the TDSE at different values of $k = -u_f(t_{rc})$ that corresponds to k_c for $M = 1836$. Compare with the exact electronic scattering matrix in Fig. 3. The three panels follow the same structure as in Fig. 11, but for different values of k. (a) Result after dividing the reconstructed nuclear wave packet just after rescattering $W_i^-(R, t_{rc})$ with the known AAnf nuclear wave packet $w_i(R, t_{rc})$ [Eq. (90)] at $T = 100$. (b) A number of these combined from $T = 60$, 100 and 140. (c) Scattering matrix obtained from a fit to the reconstructed nuclear wave packet just after rescattering at $T = 100$ using Eq. (91).

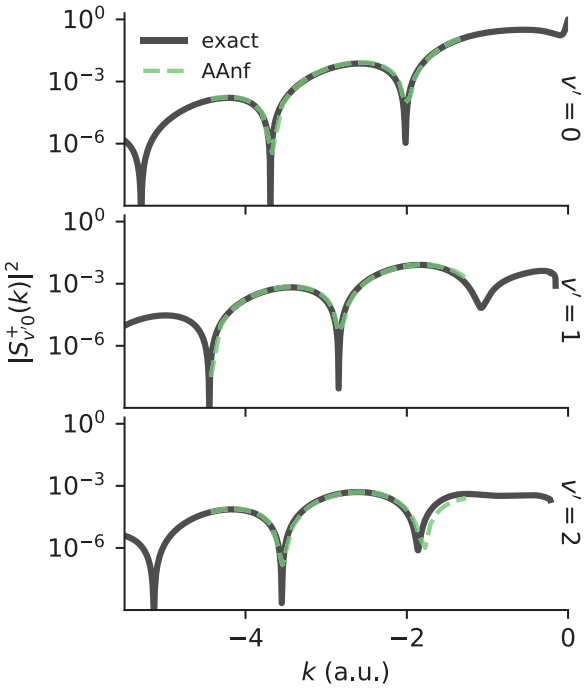

FIG. 13. Reconstruction of scattering matrix from TDSE results using Eq. (22) at different values of $k = -u_f(t_{rc})$ that corresponds to k_c for $M = 1836$. Compare with the exact scattering matrix in Fig. 2. The results are based on the fitting results in Fig. 12(c).

decay through the entire pulse at $T = 100$ and 10.1% at $T = 200$. At time t_i, the amount of decay is 0.93% and 1.96% for $T = 100$ and 200, respectively. The figure shows how the wave packet moves back and forth as T increases. The initial wave packet is defined by the product $f(R, F(t_i))\Psi(R, t_i)$ at time t_i [see Eqs. (80) and (82)]. It then moves until the time of rescattering at the caustic t_{rc}. The wave packet seems to start around the inner turning point, then spreads out, and becomes wider as it moves towards the outer turning point. When it moves back to the inner turning point, it once again becomes narrow. The time interval $t_{rc} - t_i(t_{rc})$ is proportional to T. Note that $\Psi(R, t_i)$ depends on T, so the initial nuclear wave packet is not exactly the same across different values of T, although it does not change much. In the figure we see that the width and speed of motion of the wave packet depend on nuclear mass. As expected, for smaller masses the wave packet is wider, while it is narrower for larger masses. We also see that the wave packet moves faster for smaller masses, almost finishing one period in the range of T shown for $M = 918$, while only finishing around half a period for $M = 3672$. This suggests that the speed of the wave packet scales as $1/\sqrt{M}$, as we expect for nuclear motion in the same potential. We observe larger differences between the TDSE and AAnf results for $T < 100$ at around the onset of the adiabatic regime. The agreement between the TDSE and AAnf results improves as T increases. We also observe that the norm of the reconstructed wave packet differs from the wave packet of the AAnf for $T > 150$. The difference may be due to a breakdown of the BOA, but we are not aware of the exact cause. Figure 15 illustrates the decay of the norm of the wave packet as T increases for an over-the-barrier field strength of $F_0 = 0.25$. For $T = 100$, 99.97% of the nuclear wave function $\Psi(R, t_i)$ decays across the whole pulse and 81.6% until time t_i. This decay can be seen by the norm of the nuclear wave packet decreasing as T increases. This happens since when T

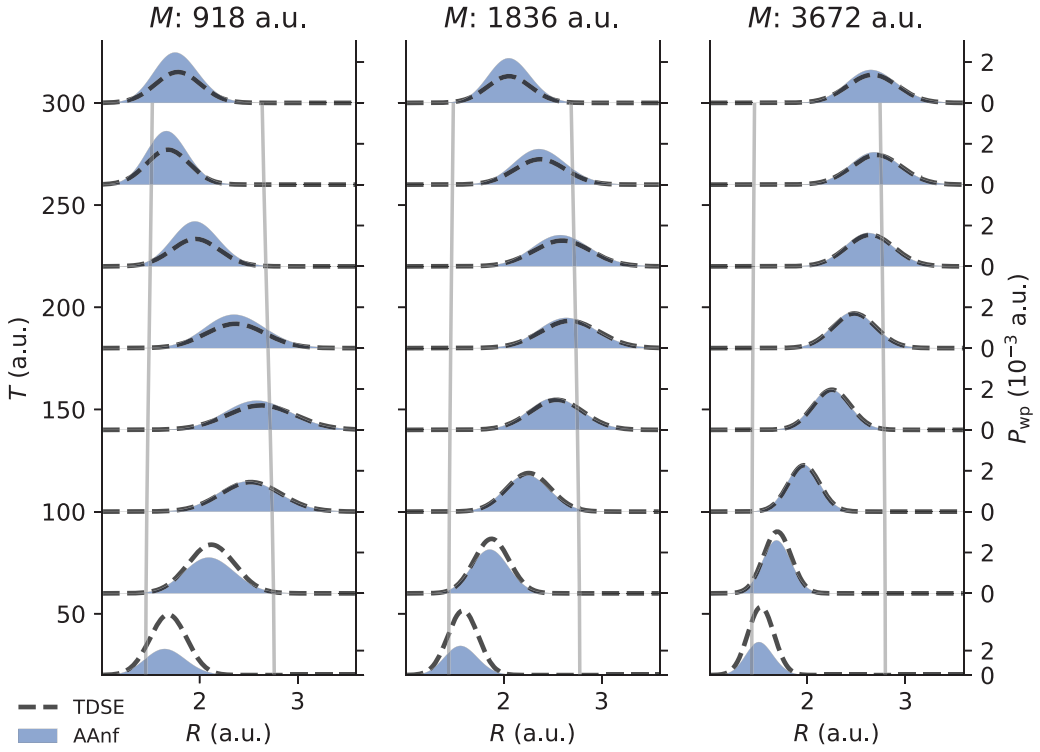

FIG. 14. Reconstruction of wave packet from TDSE results, compared to the AAnf wave packet for $F_0 = 0.1$ for different nuclear masses M. Vertical gray lines show the classical turning points of the nuclear wave packet defined as in Fig. 11 by $U_{\rm ion}(R_t) = \langle w_i|H_{\rm ion}|w_i\rangle_R/\langle w_i|w_i\rangle_R$. Note that since the molecular nuclear wave function $\Psi(R, t_i)$ depends on T, these turning points also depend weakly on T.

increases, the electron has more time to escape before the time of ionization $t_i(t_{rc})$.

Let us recall that one of the goals of Sec. V was to demonstrate the quantitative performance of the adiabatic theory by comparing its predictions with accurate numerical results obtained by solving the TDSE (31). We close this section by emphasizing that to achieve the level of agreement demonstrated in Figs. 6–15 the accurate description of molecular scattering states and the electronic SS needed to implement the theory is crucial.

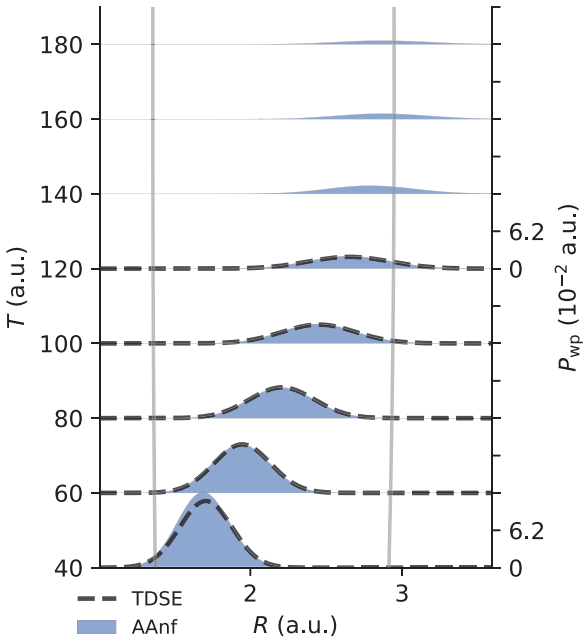

FIG. 15. Reconstruction of wave packet from the TDSE, compared to the AAnf wave packet for $M = 1836$ and $F_0 = 0.25$, plotted in the same style as in Fig. 14.

VI. MOLECULAR IMAGING USING FEW-CYCLE CEP-CONTROLLED PULSES

In this section we illustrate our procedure for reconstruction of the electronic scattering matrix using a realistic few-cycle pulse by varying the CEP. This procedure is inspired by the existing experiments for reconstruction of atomic differential cross sections in Refs. [57,64]. We consider few-cycle pulses of the form

$$F(t) = F_0 \exp(-\tau^2)\cos(\omega t - \phi), \quad \tau = \frac{2t}{T}, \tag{93}$$

where ϕ is the CEP and $\omega = 2\pi n_{\rm oc}/T$, with $n_{\rm oc}$ the number of optical cycles. The kinematics of this few-cycle pulse are somewhat more complicated than for the one-cycle pulse considered above. There are now many BRCs. The position of k_c and the corresponding u_f for all BRCs change continuously as the CEP changes. We focus on one particular BRC in a range of CEPs to reconstruct the scattering matrix in a range of u_f.

We perform TDSE and AAnf calculations for $T = 330.7$ and $n_{\rm oc} = 2$, where $\omega = 0.0380$ corresponding to a wavelength of 1200 nm. We estimate $T_f = T/n_{\rm oc} = 165$, which is well in the adiabatic regime. In the AAnf calculations, we only consider the rescattering IRTs for which ionization and

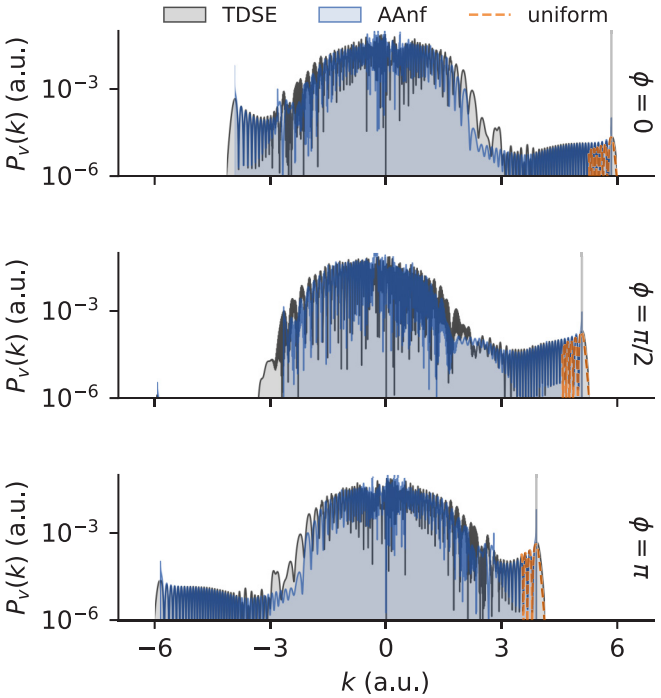

FIG. 16. The PEMD for a few-cycle pulse (93) with $T = 330.7$, $n_{oc} = 2$, and $F_0 = 0.1$ for $v = 0$. The vertical gray lines show the momentum at the caustic k_c.

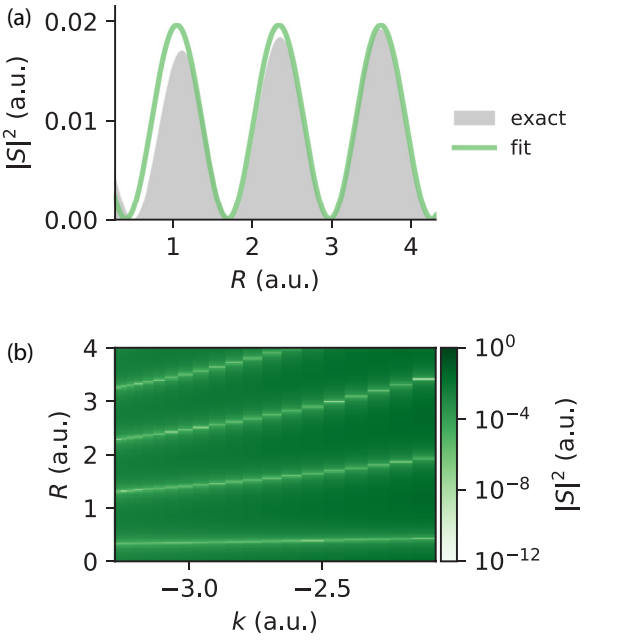

FIG. 17. Reconstructed scattering matrix from the few-cycle pulse (93) at $F_0 = 0.1$, based on fitting. The plotting style is the same as in Figs. 11(c) and 12(c). (a) Results for $\phi = 0$. The values of ϕ used in (b) are equidistantly sampled, meaning that the values of $k = u_f(t_{rc})$ are not equidistantly spaced.

rescattering are connected by a one-loop CRT, as mentioned at the end of Sec. IV B. Figure 16 shows examples of the PEMDs obtained for three representative values of ϕ. Adiabatic contributions dominate for $|k| \lesssim 2.6$. The PEMD for $|k| \gtrsim 2.6$ thus results essentially from the rescattering terms. We see that the agreement between the TDSE and AAnf results is pretty good in the regions leading up to the maximal $|k|$ at the outermost caustics. For some smaller $|k|$, the agreement is not so good, likely due to contributions from higher-order terms that we do not consider in the AAnf calculations.

We have chosen a specific caustic to track for the present reconstruction of the scattering matrix. In Fig. 16 we indicate this caustic with a vertical gray line and plot the uniform AAnf result around it. It is the most prominent caustic at positive k in the range of $0 \leqslant \phi \leqslant 5\pi/4$. Note the symmetry of $P_v(k)$ with respect to ϕ, namely, $P_v(k)$ for ϕ, is the same as $P_v(-k)$ for $\phi + \pi$. For the reconstruction in Fig. 17 we considered the PEMDs in a range of $0 \leqslant \phi \leqslant 5\pi/4$. For $\phi > 5\pi/4$, the caustic disappears, embedded into a region dominated by the adiabatic terms, and its yield is completely drowned out. For $\phi < 0$, $u_f(t_{rc})$ returns to the same values that it has already covered, which makes those values redundant for reconstructing the scattering matrix. The result of reconstructing the scattering matrix at this caustic using the fitting method from Sec. V D is depicted in Fig. 17. Good agreement is seen between the reconstruction and the known exact scattering matrix in Fig. 17(a) for $\phi = 0$, similar to the agreement in Fig. 11. In Fig. 17(b) the scattering matrix is extracted for a wide range of k and R values. The reconstruction agrees well with the exact electronic scattering matrix in Fig. 3 and the reconstructed electronic scattering matrix for the one-cycle pulse in Fig. 12.

VII. CONCLUSION

In this paper we have completed the development of the adiabatic theory of strong-field ionization of molecules including nuclear motion initiated in Ref. [44] by extending it to rescattering processes. The main results incorporating rescattering into the theory are the asymptotics of the rescattering parts of the solution to the TDSE given by Eq. (62) and the ionization amplitude given by Eqs. (67), (71), and (68), which complement the corresponding asymptotics of the adiabatic parts [Eqs. (47) and (65)] obtained in Ref. [44]. The resulting formulas define vibrationally resolved PEMDs in the whole range of the photoelectron momentum. Using the BOA for molecular scattering states and scattering matrix, we have shown that the ionization dynamics of the nuclear subsystem can be described in terms of a nuclear wave packet in the molecular ion created as a result of ionization of the molecule [Eq. (80)], its evolution until rescattering [Eq. (82)], and a nuclear wave packet after rescattering [Eq. (84)]. Furthermore, we have obtained a uniform asymptotics defining the PEMD near a backward rescattering caustic [Eq. (79)], which generalizes the factorization formula proposed in Ref. [47] and derived for systems with fixed nuclei in Ref. [65] to the situation where rescattering occurs on a parent ion having internal degrees of freedom. This result enables one to extract the nuclear wave packet after rescattering from the PEMD, from which either the scattering matrix or the nuclear wave packet before rescattering can be found. The quantitative performance of the simple and uniform asymptotics of the PEMD is illustrated by comparison with accurate calculations for a one-dimensional molecule modeling H_2. We have also demonstrated how structural and dynamic information can

be extracted from experimentally observable PEMDs using Eq. (79).

Let us mention two directions of possible further extensions of the present theory. The main process which remains not accounted for is dissociation of the molecule. However, to include dissociation one needs a wave function describing double continuum molecular states, whose construction is a problem in itself. The results of Ref. [22] suggest that such a wave function can be satisfactorily approximated using the BOA. Then dissociation can be included following Refs. [72,73]. The other direction in which the theory can be extended is to increase dimensionality of the electron. This should be possible using the method of calculating three-dimensional SSs in molecular potentials developed in Refs. [78,79].

ACKNOWLEDGMENTS

J.S. acknowledges support from the Matsuo Foundation. This work was supported in part by JSPS KAKENHI Grants No. 19H00887 and No. 21K03417.

[1] L. V. Keldysh, Ionization in the field of a strong electromagnetic wave, Zh. Eksp. Teor. Fiz. **47**, 1945 (1964); [Sov. Phys.—JETP **20**, 1307 (1965)].

[2] F. H. M. Faisal, Multiple absorption of laser photons by atoms, J. Phys. B **6**, L89 (1973).

[3] H. R. Reiss, Effect of an intense electromagnetic field on a weakly bound system, Phys. Rev. A **22**, 1786 (1980).

[4] R. Kopold, D. B. Milošević, and W. Becker, Rescattering Processes for Elliptical Polarization: A Quantum Trajectory Analysis, Phys. Rev. Lett. **84**, 3831 (2000).

[5] P. Salières, B. Carré, L. Le Déroff, F. Grasbon, G. G. Paulus, H. Walther, R. Kopold, W. Becker, D. B. Milošević, A. Sanpera, and M. Lewenstein, Feynman's path-integral approach for intense-laser-atom interactions, Science **292**, 902 (2001).

[6] A. Becker and F. H. M. Faisal, Intense-field many-body *S*-matrix theory, J. Phys. B **38**, R1 (2005).

[7] M. V. Frolov, N. L. Manakov, E. A. Pronin, and A. F. Starace, Model-Independent Quantum Approach for Intense Laser Detachment of a Weakly Bound Electron, Phys. Rev. Lett. **91**, 053003 (2003).

[8] O. I. Tolstikhin and T. Morishita, Adiabatic theory of ionization by intense laser pulses: Finite-range potentials, Phys. Rev. A **86**, 043417 (2012).

[9] D. G. Arbó, S. Yoshida, E. Persson, K. I. Dimitriou, and J. Burgdörfer, Interference Oscillations in the Angular Distribution of Laser-Ionized Electrons Near Ionization Threshold, Phys. Rev. Lett. **96**, 143003 (2006).

[10] T. Morishita, Z. Chen, S. Watanabe, and C. D. Lin, Two-dimensional electron momentum spectra of argon ionized by short intense lasers: Comparison of theory with experiment, Phys. Rev. A **75**, 023407 (2007).

[11] A. N. Grum-Grzhimailo, B. Abeln, K. Bartschat, D. Weflen, and T. Urness, Ionization of atomic hydrogen in strong infrared laser fields, Phys. Rev. A **81**, 043408 (2010).

[12] X.-F. Hou, L.-Y. Peng, Q.-C. Ning, and Q. Gong, Attosecond streaking of molecules in the low-energy region studied by a wavefunction splitting scheme, J. Phys. B **45**, 074019 (2012).

[13] I. A. Ivanov and A. S. Kheifets, Strong-field ionization of He by elliptically polarized light in attoclock configuration, Phys. Rev. A **89**, 021402(R) (2014).

[14] M. Ohmi, O. I. Tolstikhin, and T. Morishita, Analysis of a shift of the maximum of photoelectron momentum distributions generated by intense circularly polarized pulses, Phys. Rev. A **92**, 043402 (2015).

[15] O. I. Tolstikhin and T. Morishita, Strong-field ionization, rescattering, and target structure imaging with vortex electrons, Phys. Rev. A **99**, 063415 (2019).

[16] F. Krausz and M. Ivanov, Attosecond physics, Rev. Mod. Phys. **81**, 163 (2009).

[17] K. C. Kulander, F. H. Mies, and K. J. Schafer, Model for studies of laser-induced nonlinear processes in molecules, Phys. Rev. A **53**, 2562 (1996).

[18] E. A. Volkova, A. M. Popov, and O. V. Tikhonova, Two-particle one-dimensional model of the hydrogen molecular ion in an ultrashort laser pulse, JETP **83**, 889 (1996).

[19] S. Chelkowski, C. Foisy, and A. D. Bandrauk, Electron-nuclear dynamics of multiphoton H_2^+ dissociative ionization in intense laser fields, Phys. Rev. A **57**, 1176 (1998).

[20] S. Chelkowski, P. B. Corkum, and A. D. Bandrauk, Femtosecond Coulomb Explosion Imaging of Vibrational Wave Functions, Phys. Rev. Lett. **82**, 3416 (1999).

[21] S. Chelkowski, A. D. Bandrauk, A. Staudte, and P. B. Corkum, Dynamic nuclear interference structures in the Coulomb explosion spectra of a hydrogen molecule in intense laser fields: Reexamination of molecular enhanced ionization, Phys. Rev. A **76**, 013405 (2007).

[22] C. B. Madsen, F. Anis, L. B. Madsen, and B. D. Esry, Multiphoton Above Threshold Effects in Strong-Field Fragmentation, Phys. Rev. Lett. **109**, 163003 (2012).

[23] R. E. F. Silva, F. Catoire, P. Rivière, H. Bachau, and F. Martín, Correlated Electron and Nuclear Dynamics in Strong Field Photoionization of H_2^+, Phys. Rev. Lett. **110**, 113001 (2013).

[24] F. Morales, P. Rivière, M. Richter, A. Gubaydullin, M. Ivanov, O. Smirnova, and F. Martín, High harmonic spectroscopy of electron localization in the hydrogen molecular ion, J. Phys. B **47**, 204015 (2014).

[25] C. Huang, O. I. Tolstikhin, and T. Morishita, Strong-field subcycle control of dissociation dynamics via exceptional points of molecules in an electric field, Phys. Rev. A **95**, 063416 (2017).

[26] S. Chelkowski, T. Zuo, O. Atabek, and A. D. Bandrauk, Dissociation, ionization, and coulomb explosion of H_2^+ in an intense laser field by numerical integration of the time-dependent schrödinger equation, Phys. Rev. A **52**, 2977 (1995).

[27] S. Chelkowski, A. Conjusteau, T. Zuo, and A. D. Bandrauk, Dissociative ionization of H_2^+ in an intense laser field: Charge-resonance-enhanced ionization, Coulomb explosion, and harmonic generation at 600 nm, Phys. Rev. A **54**, 3235 (1996).

[28] I. Kawata, H. Kono, and Y. Fujimura, Adiabatic and diabatic responses of H_2^+ to an intense femtosecond laser pulse: Dynamics of the electronic and nuclear wave packet, J. Chem. Phys. **110**, 11152 (1999).

[29] V. Roudnev, B. D. Esry, and I. Ben-Itzhak, Controlling HD^+ and H_2^+ Dissociation with the Carrier-Envelope Phase Difference of an Intense Ultrashort Laser Pulse, Phys. Rev. Lett. **93**, 163601 (2004).

[30] V. Roudnev and B. D. Esry, HD^+ photodissociation in the scaled coordinate approach, Phys. Rev. A **71**, 013411 (2005).

[31] M. Lein, Attosecond Probing of Vibrational Dynamics with High-Harmonic Generation, Phys. Rev. Lett. **94**, 053004 (2005).

[32] G. K. Paramonov, Vibrational excitation of simple molecular ions in resonant and under-resonant strong laser fields: Dissociation and ionization of *ppe* and *pde*; laser-enhanced nuclear fusion in $dd\mu$ and $dt\mu$, Chem. Phys. **338**, 329 (2007).

[33] F. He, A. Becker, and U. Thumm, Strong-Field Modulated Diffraction Effects in the Correlated Electron-Nuclear Motion in Dissociating H_2^+, Phys. Rev. Lett. **101**, 213002 (2008).

[34] G. K. Paramonov, T. Klamroth, H. Z. Lu, and A. D. Bandrauk, Quantum dynamics, isotope effects, and power spectra of $H_2{}^+$ and HD^+ excited to the continuum by strong one-cycle laser pulses: Three-dimensional non-Born-Oppenheimer simulations, Phys. Rev. A **98**, 063431 (2018).

[35] S. Baker, J. S. Robinson, C. A. Haworth, H. Teng, R. A. Smith, C. C. Chirilă, M. Lein, J. W. G. Tisch, and J. P. Marangos, Probing proton dynamics in molecules on an attosecond time scale, Science **312**, 424 (2006).

[36] A. Staudte, D. Pavičić, S. Chelkowski, D. Zeidler, M. Meckel, H. Niikura, M. Schöffler, S. Schössler, B. Ulrich, P. P. Rajeev, T. Weber, T. Jahnke, D. M. Villeneuve, A. D. Bandrauk, C. L. Cocke, P. B. Corkum, and R. Dörner, Attosecond Strobing of Two-Surface Population Dynamics in Dissociating $H_2{}^+$, Phys. Rev. Lett. **98**, 073003 (2007).

[37] B. Feuerstein, T. Ergler, A. Rudenko, K. Zrost, C. D. Schröter, R. Moshammer, J. Ullrich, T. Niederhausen, and U. Thumm, Complete Characterization of Molecular Dynamics in Ultrashort Laser Fields, Phys. Rev. Lett. **99**, 153002 (2007).

[38] J. Wu, M. Kunitski, M. Pitzer, F. Trinter, L. P. H. Schmidt, T. Jahnke, M. Magrakvelidze, C. B. Madsen, L. B. Madsen, U. Thumm, and R. Dörner, Electron-Nuclear Energy Sharing in Above-Threshold Multiphoton Dissociative Ionization of H_2, Phys. Rev. Lett. **111**, 023002 (2013).

[39] H. Xu, T.-Y. Xu, F. He, D. Kielpinski, R. T. Sang, and I. V. Litvinyuk, Effect of nuclear mass on carrier-envelope-phase-controlled electron localization in dissociating molecules, Phys. Rev. A **89**, 041403(R) (2014).

[40] P. Lu, W. Zhang, X. Gong, Q. Song, K. Lin, Q. Ji, J. Ma, F. He, H. Zeng, and J. Wu, Electron-nuclear correlation in above-threshold double ionization of molecules, Phys. Rev. A **95**, 033404 (2017).

[41] W. Zhang, X. Gong, H. Li, P. Lu, F. Sun, Q. Ji, K. Lin, J. Ma, H. Li, J. Qiang *et al.*, Electron-nuclear correlated multiphoton-route to Rydberg fragments of molecules, Nat. Commun. **10**, 757 (2019).

[42] P. B. Corkum, Plasma Perspective on Strong Field Multiphoton Ionization, Phys. Rev. Lett. **71**, 1994 (1993).

[43] P. B. Corkum and F. Krausz, Attosecond science, Nat. Phys. **3**, 381 (2007).

[44] J. Svensmark, O. I. Tolstikhin, and T. Morishita, Adiabatic theory of strong-field ionization of molecules including nuclear motion, Phys. Rev. A **101**, 053422 (2020).

[45] G. G. Paulus, W. Becker, W. Nicklich, and H. Walther, Rescattering effects in above-threshold ionization: A classical model, J. Phys. B **27**, L703 (1994).

[46] M. Meckel, D. Comtois, D. Zeidler, A. Staudte, D. Pavicic, H. C. Bandulet, H. Pepin, J. C. Kieffer, R. Dorner, D. M. Villeneuve, and P. B. Corkum, Laser-Induced Electron Tunneling and Diffraction, Science **320**, 1478 (2008).

[47] T. Morishita, A.-T. Le, Z. Chen, and C. D. Lin, Accurate Retrieval of Structural Information from Laser-Induced Photoelectron and High-Order Harmonic Spectra by Few-Cycle Laser Pulses, Phys. Rev. Lett. **100**, 013903 (2008).

[48] M. Okunishi, T. Morishita, G. Prümper, K. Shimada, C. D. Lin, S. Watanabe, and K. Ueda, Experimental Retrieval of Target Structure Information from Laser-Induced Rescattered Photoelectron Momentum Distributions, Phys. Rev. Lett. **100**, 143001 (2008).

[49] D. Ray, B. Ulrich, I. Bocharova, C. Maharjan, P. Ranitovic, B. Gramkow, M. Magrakvelidze, S. De, I. V. Litvinyuk, A. T. Le, T. Morishita, C. D. Lin, G. G. Paulus, and C. L. Cocke, Large-Angle Electron Diffraction Structure in Laser-Induced Rescattering from Rare Gases, Phys. Rev. Lett. **100**, 143002 (2008).

[50] S. Micheau, Z. Chen, A. T. Le, J. Rauschenberger, M. F. Kling, and C. D. Lin, Accurate Retrieval of Target Structures and Laser Parameters of Few-Cycle Pulses from Photoelectron Momentum Spectra, Phys. Rev. Lett. **102**, 073001 (2009).

[51] D. B. Milošević, W. Becker, M. Okunishi, G. Prümper, K. Shimada, and K. Ueda, Strong-field electron spectra of rare-gas atoms in the rescattering regime: Enhanced spectral regions and a simulation of the experiment, J. Phys. B **43**, 015401 (2009).

[52] M. Okunishi, H. Niikura, R. R. Lucchese, T. Morishita, and K. Ueda, Extracting Electron-Ion Differential Scattering Cross Sections for Partially Aligned Molecules by Laser-Induced Rescattering Photoelectron Spectroscopy, Phys. Rev. Lett. **106**, 063001 (2011).

[53] C. I. Blaga, J. Xu, A. D. DiChiara, E. Sistrunk, K. Zhang, P. Agostini, T. A. Miller, L. F. DiMauro, and C. D. Lin, Imaging ultrafast molecular dynamics with laser-induced electron diffraction, Nature (London) **483**, 194 (2012).

[54] J. Xu, C. I. Blaga, A. D. DiChiara, E. Sistrunk, K. Zhang, Z. Chen, A.-T. Le, T. Morishita, C. D. Lin, P. Agostini, and L. F. DiMauro, Laser-Induced Electron Diffraction for Probing Rare Gas Atoms, Phys. Rev. Lett. **109**, 233002 (2012).

[55] J. Xu, C. I. Blaga, K. Zhang, Y. H. Lai, C. D. Lin, T. A. Miller, P. Agostini, and L. F. DiMauro, Diffraction using laser-driven broadband electron wave packets, Nat. Commun. **5**, 4635 (2014).

[56] B. Wolter, M. G. Pullen, M. Baudisch, M. Sclafani, M. Hemmer, A. Senftleben, C. D. Schröter, J. Ullrich, R. Moshammer, and J. Biegert, Strong-Field Physics with Mid-IR Fields, Phys. Rev. X **5**, 021034 (2015).

[57] H. Geiseler, N. Ishii, K. Kaneshima, F. Geier, T. Kanai, O. I. Tolstikhin, T. Morishita, and J. Itatani, Carrier-envelope phase mapping in laser-induced electron diffraction, Phys. Rev. A **94**, 033417 (2016).

[58] B. Wolter, M. G. Pullen, A.-T. Le, M. Baudisch, K. Doblhoff-Dier, A. Senftleben, M. Hemmer, C. D. Schröter, J. Ullrich,

T. Pfeifer, R. Moshammer, S. Gräfe, O. Vendrell, C. D. Lin, and J. Biegert, Ultrafast electron diffraction imaging of bond breaking in di-ionized acetylene, Science **354**, 308 (2016).

[59] S. G. Walt, N. Bhargava Ram, M. Atala, N. I. Shvetsov-Shilovski, A. von Conta, D. Baykusheva, M. Lein, and H. J. Wörner, Dynamics of valence-shell electrons and nuclei probed by strong-field holography and rescattering, Nat. Commun. **8**, 15651 (2017).

[60] Y. Ito, M. Okunishi, T. Morishita, O. I. Tolstikhin, and K. Ueda, Rescattering photoelectron spectroscopy of heterodiatomic molecules with an analytical returning photoelectron wave packet, Phys. Rev. A **97**, 053411 (2018).

[61] K. Amini, M. Sclafani, T. Steinle, A.-T. Le, A. Sanchez, C. Müller, J. Steinmetzer, L. Yue, J. R. Martínez Saavedra, M. Hemmer, M. Lewenstein, R. Moshammer, T. Pfeifer, M. G. Pullen, J. Ullrich, B. Wolter, R. Moszynski, F. J. García de Abajo, C. D. Lin, S. Gräfe *et al.*, Imaging the Renner–Teller effect using laser-induced electron diffraction, Proc. Natl. Acad. Sci. USA **116**, 8173 (2019).

[62] M. Okunishi, Y. Ito, V. Sharma, S. Aktar, K. Ueda, R. R. Lucchese, A. I. Dnestryan, O. I. Tolstikhin, S. Inoue, H. Matsui, and T. Morishita, Rescattering photoelectron spectroscopy of the CO_2 molecule: Progress towards experimental discrimination between theoretical target-structure models, Phys. Rev. A **100**, 053404 (2019).

[63] B. Belsa, K. Amini, X. Liu, A. Sanchez, T. Steinle, J. Steinmetzer, A. T. Le, R. Moshammer, T. Pfeifer, J. Ullrich, R. Moszynski, C. D. Lin, S. Gräfe, and J. Biegert, Laser-induced electron diffraction of the ultrafast umbrella motion in ammonia, Struct. Dyn. **8**, 014301 (2021).

[64] T. Mizuno, N. Ishii, T. Kanai, P. Rosenberger, D. Zietlow, M. F. Kling, O. I. Tolstikhin, T. Morishita, and J. Itatani, Observation of the quantum shift of a backward rescattering caustic by carrier-envelope phase mapping, Phys. Rev. A **103**, 043121 (2021).

[65] T. Morishita and O. I. Tolstikhin, Adiabatic theory of strong-field photoelectron momentum distributions near a backward rescattering caustic, Phys. Rev. A **96**, 053416 (2017).

[66] H. Niikura, F. Légaré, R. Hasbani, A. D. Bandrauk, M. Y. Ivanov, D. M. Villeneuve, and P. B. Corkum, Sub-laser-cycle electron pulses for probing molecular dynamics, Nature (London) **417**, 917 (2002).

[67] S. Patchkovskii and M. S. Schuurman, Full-dimensional treatment of short-time vibronic dynamics in a molecular high-order-harmonic-generation process in methane, Phys. Rev. A **96**, 053405 (2017).

[68] Y. Zhou, O. I. Tolstikhin, and T. Morishita, Near-Forward Rescattering Photoelectron Holography in Strong-Field Ionization: Extraction of the Phase of the Scattering Amplitude, Phys. Rev. Lett. **116**, 173001 (2016).

[69] K. Liu, S. Luo, M. Li, Y. Li, Y. Feng, B. Du, Y. Zhou, P. Lu, and I. Barth, Detecting and Characterizing the Nonadiabaticity of Laser-Induced Quantum Tunneling, Phys. Rev. Lett. **122**, 053202 (2019).

[70] O. I. Tolstikhin and L. B. Madsen, Retardation Effects and the Born-Oppenheimer Approximation: Theory of Tunneling Ionization of Molecules Revisited, Phys. Rev. Lett. **111**, 153003 (2013).

[71] J. Svensmark, O. I. Tolstikhin, and L. B. Madsen, Coulomb and dipole effects in tunneling ionization of molecules including nuclear motion, Phys. Rev. A **91**, 013408 (2015).

[72] J. Svensmark, O. I. Tolstikhin, and L. B. Madsen, Theory of dissociative tunneling ionization, Phys. Rev. A **93**, 053426 (2016).

[73] J. Svensmark, O. I. Tolstikhin, and L. B. Madsen, Bound and continuum energy distributions of nuclear fragments resulting from tunneling ionization of molecules, Phys. Rev. A **97**, 033408 (2018).

[74] H. Wind, Electron energy for H_2^+ in the ground state, J. Chem. Phys. **42**, 2371 (1965).

[75] K. Pachucki, Born-Oppenheimer potential for H_2, Phys. Rev. A **82**, 032509 (2010).

[76] L. D. Landau and E. M. Lifshitz, *Quantum Mechanics: Non-Relativistic Theory* (Pergamon, Oxford, 1977).

[77] H. Gao and C. H. Greene, Alternative vibrational frame transformation for electron-molecule scattering, Phys. Rev. A **42**, 6946 (1990).

[78] P. A. Batishchev, O. I. Tolstikhin, and T. Morishita, Atomic Siegert states in an electric field: Transverse momentum distribution of the ionized electrons, Phys. Rev. A **82**, 023416 (2010).

[79] L. Hamonou, T. Morishita, and O. I. Tolstikhin, Molecular Siegert states in an electric field, Phys. Rev. A **86**, 013412 (2012).

[80] F. H. M. Faisal and S. Förster, Coulomb-Volkov S-matrix theory of ionisation, J. Phys. B **51**, 234001 (2018).

[81] R. P. Feynman and A. R. Hibbs, *Quantum Mechanics and Path Integrals* (McGraw-Hill, New York, 1965).

[82] G. D. Dickenson, M. L. Niu, E. J. Salumbides, J. Komasa, K. S. E. Eikema, K. Pachucki, and W. Ubachs, Fundamental Vibration of Molecular Hydrogen, Phys. Rev. Lett. **110**, 193601 (2013).

[83] O. I. Tolstikhin, T. Morishita, and S. Watanabe, Adiabatic theory of ionization of atoms by intense laser pulses: One-dimensional zero-range-potential model, Phys. Rev. A **81**, 033415 (2010).

[84] D. B. Milošević, Low-frequency approximation for above-threshold ionization by a laser pulse: Low-energy forward rescattering, Phys. Rev. A **90**, 063423 (2014).

[85] M. Abramowitz and I. A. Stegun, *Handbook of Mathematical Functions* (Dover, New York, 1972).

[86] M. Busuladžić, A. Gazibegović-Busuladžić, and D. B. Milošević, High-order above-threshold ionization in a laser field: Influence of the ionization potential on the high-energy cutoff, Laser Phys. **16**, 289 (2006).